

Soft, stretchable, fully implantable miniaturized optoelectronic systems for wireless optogenetics

Sung Il Park^{1,2,8}, Daniel S Brenner^{3,8}, Gunchul Shin^{1,2,8}, Clinton D Morgan^{3,8}, Bryan A Copits³, Ha Uk Chung^{1,2}, Melanie Y Pullen³, Kyung Nim Noh^{1,2}, Steve Davidson³, Soong Ju Oh^{1,4}, Jangyeol Yoon^{1,2,5}, Kyung-In Jang^{1,2}, Vijay K Samineni³, Megan Norman³, Jose G Grajales-Reyes³, Sherri K Vogt³, Saranya S Sundaram³, Kellie M Wilson³, Jeong Sook Ha⁵, Renxiao Xu⁶, Taisong Pan⁶, Tae-il Kim⁷, Yonggang Huang⁶, Michael C Montana³, Judith P Golden³, Michael R Bruchas³, Robert W Gereau IV³ & John A Rogers^{1,2}

Optogenetics allows rapid, temporally specific control of neuronal activity by targeted expression and activation of light-sensitive proteins. Implementation typically requires remote light sources and fiber-optic delivery schemes that impose considerable physical constraints on natural behaviors. In this report we bypass these limitations using technologies that combine thin, mechanically soft neural interfaces with fully implantable, stretchable wireless radio power and control systems. The resulting devices achieve optogenetic modulation of the spinal cord and peripheral nervous system. This is demonstrated with two form factors; stretchable film appliquéés that interface directly with peripheral nerves, and flexible filaments that insert into the narrow confines of the spinal epidural space. These soft, thin devices are minimally invasive, and histological tests suggest they can be used in chronic studies. We demonstrate the power of this technology by modulating peripheral and spinal pain circuitry, providing evidence for the potential widespread use of these devices in research and future clinical applications of optogenetics outside the brain.

The use of optogenetics in the brain has revolutionized the interrogation of neural circuitry by enabling temporal and spatial control of neuronal function. However, attempts to apply optogenetic studies to tissues beyond the brain have been stymied by the inability to target peripheral and spinal circuits in freely moving animals. Studies to date have primarily used cumbersome tethered fiber-optic cables or light emitting diode (LED) arrays to activate opsins that are expressed transgenically or delivered through gene therapy^{1–3}. Although these experimental approaches have utility, physical tethers impede movement, which can alter behavior and the natural motion of animals in complex environments. Additionally, the fixation of fiber-optic cables requires physical bonding to a static skeletal feature such as the skull, and external fixtures can cause device loss due to damage by the animal, a cage mate, or by inadvertent damage from housing.

These fibers can also damage the surrounding neural tissue during insertion or during fiber coupling owing to relative motion of the hard fiber against soft tissues^{4,5}.

Thin, injectable polymer filaments with integrated, cellular-scale LEDs and externally mounted, wireless power-harvesting systems^{6–9} represent attractive alternatives, but cannot illuminate spatially challenging and highly mobile areas like peripheral nerves or the spinal cord, which are critical to the study of the extracranial circuits involved in sensory input and motor output. Recently developed fully implantable devices with radio frequency (RF)-powered LEDs achieve some capabilities in these contexts¹⁰; however, these devices use hard materials and geometrically thick designs, which limit their potential for chronic biocompatibility and integration with soft tissues of the nervous system.

Miniaturized, biocompatible devices that can safely interface with peripheral neural tissue and illuminate challenging areas are needed to advance the technology support for advanced optogenetic studies not only of the brain, but also of issues related to chronic pain, itch and other neurological disorders. The development of suitable devices requires management of heat generation and power delivery; robust remote activation with uniform, natural operation across cage configurations and animal species; power delivery over large areas; and miniaturization with thin geometries and low-modulus, elastic mechanics for chronic tissue compatibility⁸.

Here we present miniaturized, soft wireless optoelectronic systems with versatile layout options that are fully compatible with advanced methods for mass production in semiconductor device manufacturing and capable of complete, minimally invasive implantation over multiple neural interfaces. The low-modulus mechanics of these biocompatible devices allows their implantation as thin appliquéés and/or soft injectable filaments, without the need for skeletal fixation, thereby permitting experiments in regions where it would be impossible to operate with other approaches. We demonstrate that these devices can specifically and reversibly activate both peripheral and spinal pain

¹Department of Materials Science and Engineering, University of Illinois at Urbana-Champaign, Urbana, Illinois, USA. ²Frederick Seitz Materials Research Laboratory, University of Illinois at Urbana-Champaign, Urbana, Illinois, USA. ³Washington University Pain Center and Department of Anesthesiology, Washington University School of Medicine, St. Louis, Missouri, USA. ⁴Department of Materials Science and Engineering, Korea University, Seoul, Republic of Korea. ⁵Department of Chemical and Biological Engineering, Korea University, Seoul, Republic of Korea. ⁶Department of Mechanical Engineering, Northwestern University, Chicago, Illinois, USA. ⁷School of Chemical Engineering, Sungkyunkwan University (SKKU), Suwon, Republic of Korea. ⁸These authors contributed equally to this work. Correspondence should be addressed to J.A.R. (jrogers@illinois.edu) or R.W.G. (gereau@wustl.edu).

Received 12 March; accepted 22 October; published online 9 November 2015; doi:10.1038/nbt.3415

circuits in freely moving, untethered mice. Detailed chronic studies and histological evaluations show the essential benefits of soft, compliant and fully implantable device technologies of this type.

Our miniaturized wireless optoelectronic systems were composed of an RF harvesting unit that receives signals from a transmitter, rectifies them, multiplies the voltages and routes the resulting direct-current output to the LEDs (a turn-on voltage of 2.7 V, 470 nm wavelength). The antenna and LEDs are connected with serpentine Ti/Au electrical interconnects, and the circuit is encapsulated by polyimide (40 μm width, 3 μm thickness) and a low-modulus silicone elastomer (~0.5 MPa, 100 μm thickness). This process yields soft, system-level mechanics (effective modulus of ~1.7 MPa) capable of accommodating anatomical shapes and natural motions^{6–9} (Fig. 1a, Supplementary Note 1, Supplementary Figs. 1–3 and Supplementary Table 1).

The mechanical compliance, miniaturized geometry (0.7 mm \times 3.8 mm \times 6 mm) and lightweight construction (16 mg) of these devices enabled implantation into anatomical regions that were previously inaccessible owing to physical constraints. In comparison with previous technology, these devices are substantially thinner, softer and more flexible (Supplementary Note 1)^{8,10,11}. We deployed these devices underneath muscle for optogenetic stimulation of a peripheral nerve (Fig. 1b), and in the epidural space for optogenetic control in the spinal cord (Fig. 1c). Peripheral nerve illumination was achieved with a soft appliqué that was implanted with the antenna in a subcutaneous pocket with an LED extension that traverses under the gluteus maximus to the sciatic nerve. The distal extension with the LEDs included wings (1 mm \times 3 mm) that anchored the LED tip in the gluteal pocket once the muscular architecture had been repaired with suture (Fig. 1b,d,f). Spinal illumination was achieved

by implantation under the vertebra in the epidural space, which was accessed by laminectomy of the T13 spinous process (Fig. 1c,e,g). This placement centered the narrow part of the device (380 μm \times 8 mm) over the lumbar spinal cord.

The key to miniaturizing these devices is a stretchable antenna that harvests RF power through capacitive coupling between adjacent serpentine traces (Supplementary Fig. 4), thereby lowering the resonant frequency and therefore the dimensions of the antenna¹². For operation at 2.34 GHz, this design required an area of only 3 \times 3 mm, a 100-fold reduction in volume and weight compared to conventional rigid antennas⁸. This antenna also featured a wide bandwidth, which is essential for reliable activation of the devices as the center frequency of the receiving antenna must be similar to that of the transmitting antenna to efficiently harvest transmitted power. The center frequency describes the frequency range where an antenna absorbs energy most effectively and corresponds to the range of frequencies that minimize the scattering parameter (S_{11}). A lower S_{11} indicates that less incident energy is reflected off the antenna and therefore more of that energy is absorbed. The wide bandwidth (200 MHz) of the stretchable antenna allows it to harvest RF power from a much wider range of transmitting frequencies than conventional patch antennae (bandwidth of 50 MHz) (Supplementary Fig. 4d). This characteristic reduces the likelihood that a mismatch between the receiver and transmitter will prevent device activation. The S_{11} and center frequency in these devices are also affected by the physiological environment (Supplementary Note 2 and Supplementary Fig. 5).

The capacitive coupling that powers these devices can be diminished if strain deforms the metallized traces and increases the sizes of the gaps between them. To assess the reliability of these antennae under

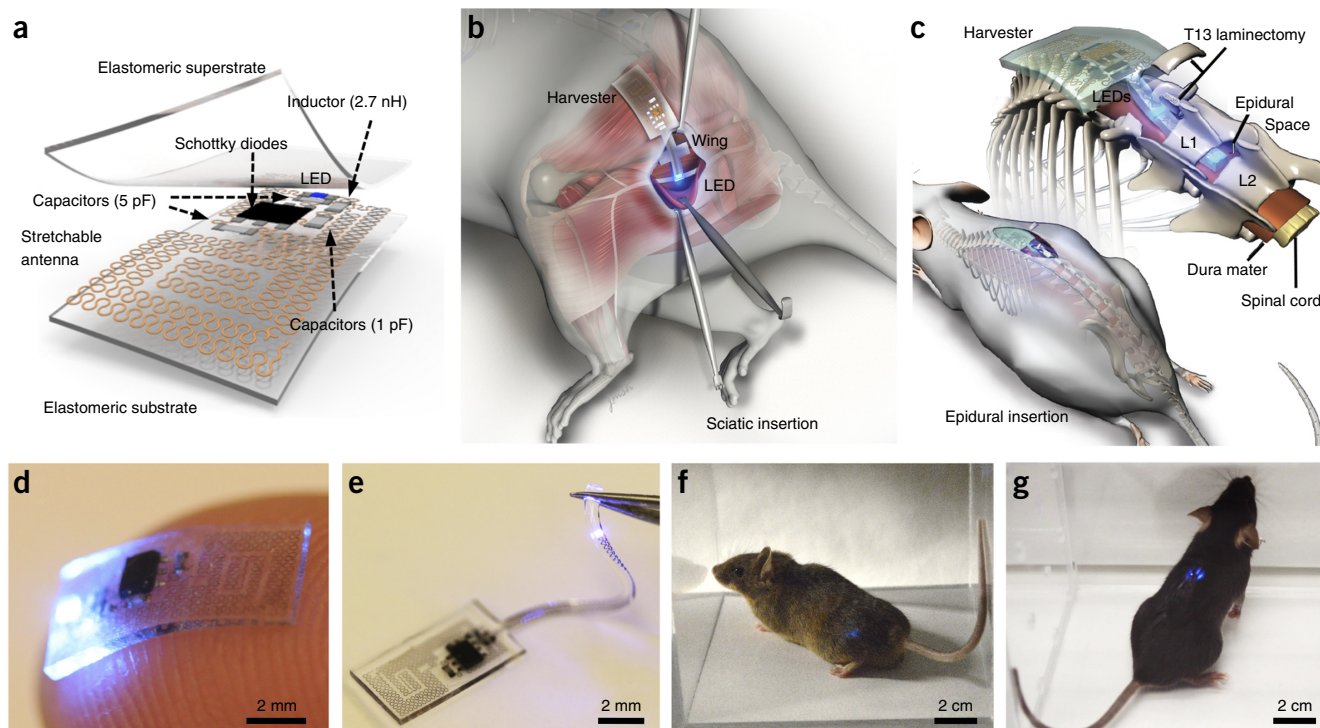
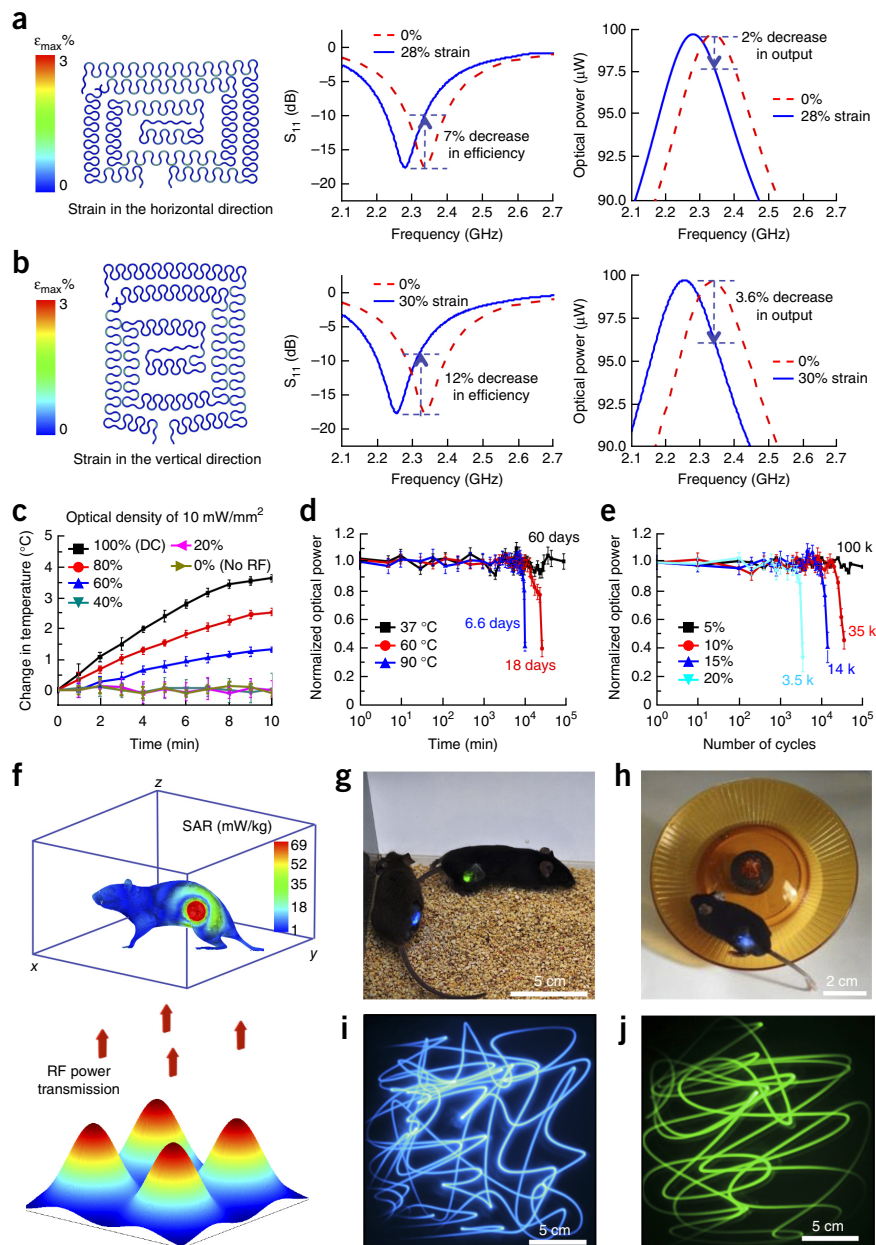


Figure 1 Miniaturized, fully implantable, soft optoelectronic systems for wireless optogenetics. (a) Exploded view schematic illustration of the energy harvester component of the system, with an integrated LED to illustrate operation. (b,c) The anatomy and location of the peripheral and epidural devices relative to the sciatic nerve (b) and spinal cord (c). (d) Picture of an active device resting on the tip of the index finger. The device is 0.7 mm thick, 3.8 mm wide and 6 mm long; its weight is 16 mg. (e) Picture of the epidural device, highlighting the soft, stretchable connection to an LED. The diameter of the epidural implant component is 380 μm , with cross sectional dimensions comparable to the epidural space. (f,g) Mice with wireless devices implanted near the sciatic nerve (f) and the spinal cord (g).

Figure 2 Electrical and mechanical characteristics of the stretchable optoelectronics systems. **(a,b)** Strain distributions in the stretchable antenna (left), its scattering coefficient S_{11} (middle), and corresponding optical output power (right) for strain applied in the horizontal (28%) **(a)** and vertical directions (30%) **(b)**, and for the undeformed (0%) configuration (red dashed). **(c)** *In vivo* monitoring of the temperature of a mouse at the location of an implanted device using infrared imaging, during device operation. **(d)** Measurements of optical output power from devices operating while immersed in saline at temperatures of 37 °C, 60 °C and 90 °C as a function of time. **(e)** Measurements of optical output power from devices subjected to cyclical application of strain with magnitudes between 5% and 20%. **(f)** Schematic illustration of the TX system and an experimental assay with computed SAR distributions on a mouse mesh body. Multiple antennas lie in the xy plane, placed below the assay. **(g)** Simultaneous operation of devices implanted into multiple animals in the same cage (30 × 30 cm). **(h)** A mouse running on a wheel with a device interfaced to the sciatic nerve. **(i,j)** Long-exposure pictures of continuous activation of LED devices manually moved through the enclosure.



biological strain, we modeled and tested performance under worst-case scenarios (30% strain) (Fig. 2a,b and Supplementary Fig. 5). Simulations showed that although uniaxial strains of ~10% increased the gap size in the direction of the strain, they reduced the gap size in the orthogonal direction by up to 50% (Supplementary Fig. 6). As a result, the decrease in coupling owing to increased gap size was balanced by enhanced coupling in the orthogonal direction, such that the harvesting efficiency of the antenna was largely unaffected (Fig. 2a,b).

Although strain does not alter the efficiency of capacitive coupling, it does shift the center frequency of the antenna toward lower frequencies (Fig. 2a,b). However, the magnitudes of the strain-induced shifts in the center frequency were small compared to the large bandwidth (Supplementary Fig. 4d), such that the net result of supraphysiological strain application was a 12% decrease in coupling efficiency due to center frequency shifts (Fig. 2a,b middle). This translates to a modeled optical power output decrease of only a few percent, suggesting that physiological strain is unlikely to significantly impair device function (Fig. 2a,b, right). We confirmed this modeling by testing devices under deformation conditions that greatly exceeded anything expected to occur in animals; the devices functioned reliably (Fig. 2h, Supplementary Fig. 7). Additionally, a mouse with a device interfaced to the sciatic nerve ran without trouble on an exercise wheel (Supplementary Fig. 8 and Supplementary Movie 1) and 6 months after implantation a wireless device still functioned in another mouse (Fig. 1f), providing evidence that these devices function reliably under physiological strain.

In addition to physical strain, other concerns for long-term implantation of electrical devices in animals include heat generation and

long-term durability. Infrared imaging of an anesthetized mouse during device operation revealed that an optical power density of 10 mW/mm² (40% duty cycle; 20 Hz period; 20 ms pulse width) does not cause detectable temperature changes (Fig. 2c). Studies using implantable thermal sensors showed similar trends (Supplementary Fig. 9 and Supplementary Note 3). Exposure to biological conditions did not greatly alter device operation or durability; devices retained full functionality for 2 months when immersed in 37 °C saline, and for 6 days in saline at supraphysiological temperatures (90 °C) (Fig. 2d). In terms of mechanical stability, these devices were cycled >10⁵ times without a detectable loss in optical power (Fig. 2e). The robustness suggested in these *in vitro* assays is reinforced by the fact that 76% (31/41) of devices that were implanted for use in this work were still functional in the animals after 1 week. Two sciatic nerve devices retained reliable activation at least every month for 6 months after implantation; additionally, and of five sciatic nerve devices where we attempted reimplantation in new host mice after initial removal,

three remained functional for 3 weeks after reimplantation. All of these observations suggest that heat generation, hydration effects and durability are not obstacles for the use of these devices in animals.

For the devices to be useful in behavior experiments, the RF transmission (TX) systems must enable continuous operation throughout

a location of interest (e.g., the home cage or testing arena), at field strengths that lie below IEEE and Federal Communications Commission (FCC) guidelines. A configuration of four TX antennas connected to a common RF power supply (Fig. 2f) provided total average RF power that was sufficient for operation (~2 W) throughout the

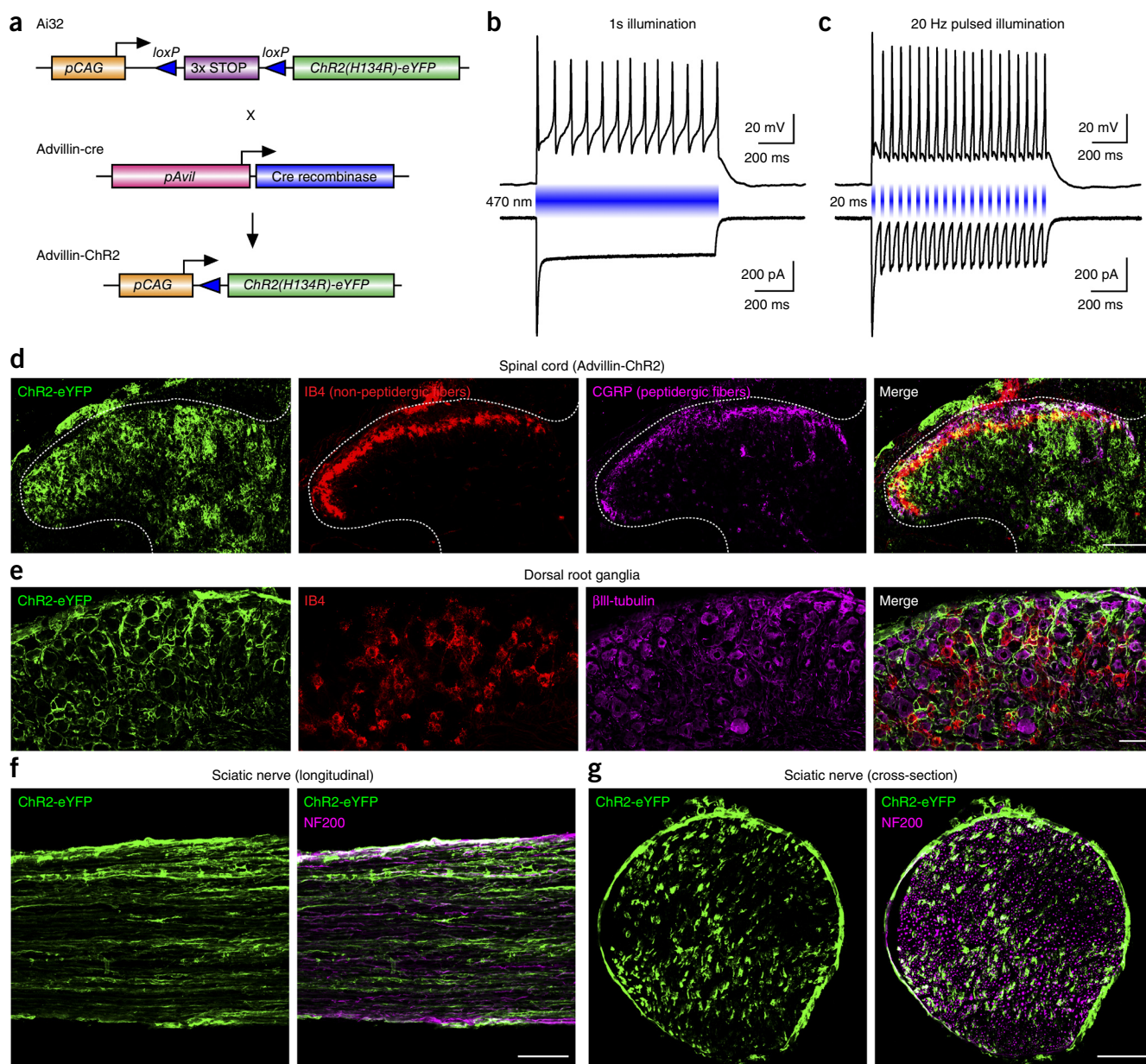
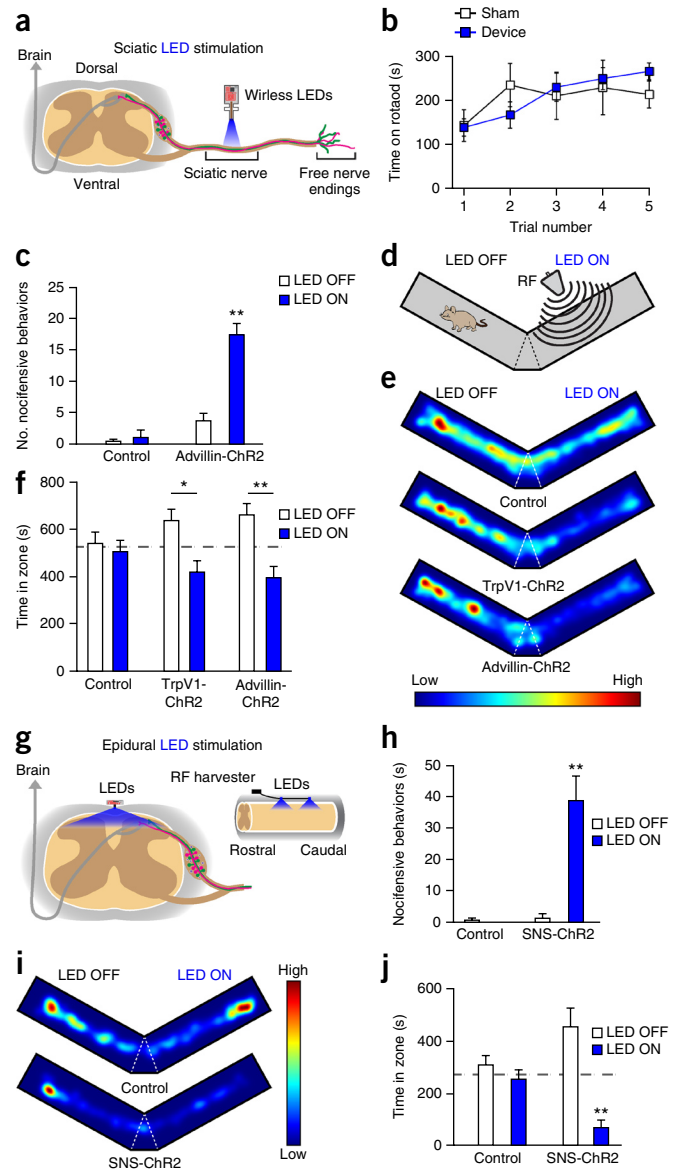


Figure 3 Electrophysiological and anatomical characterization of ChR2 expression in Advillin-ChR2 mice. **(a)** Schematic of the Ai32 locus and Advillin-cre mouse locus where stop codons are inserted in all three reading frames and flanked by *loxP* sites upstream of the coding region for ChR2. The Advillin-cre mouse locus shows cre-recombinase driven by the sensory neuron-specific *Avil* promoter. Cre recombinase expression results in recombination between *loxP* sites and excision of the stop codons, leading to expression of ChR2. Electrophysiological recordings from DRG neurons cultured from Advillin-ChR2 mice. For all traces, 470-nm illumination is delivered at 10 mW/mm². **(b)** 1-second-long illumination induces inward currents (lower trace) in voltage clamp recordings, and in some cells produces sustained firing in current clamp recordings (upper trace). **(c)** Pulsed illumination at 20 Hz induces action potential firing with high fidelity (upper trace) resulting from the inward currents that are generated in voltage clamp (lower trace). Note that the first pulse produces larger amplitude inward currents relative to the second and all subsequent light pulses, consistent with the rapid desensitization to a steady-state current seen with prolonged illumination (**b**, lower). **(d)** Immunohistochemical analysis of tissue from adult Advillin-ChR2 mice demonstrates that ChR2 is expressed along the peripheral neuraxis, including termination in lamina I and lamina II of the spinal cord dorsal horn as evidenced by overlap with CGRP (purple) and IB4 (red), respectively. **(e)** Staining of DRG shows considerable overlap of ChR2 expression with the neuronal marker β III tubulin (purple) and IB4 (red) within the soma. **(f, g)** Longitudinal (**f**) and cross-sections (**g**) of sciatic nerve demonstrate robust staining along the plasma membrane of the axons of both myelinated (marked with NF200, purple) and unmyelinated neurons, and some expression of ChR2 in the circumferential nonexcitable epineurial tissue. Scale bars, 100 μ m for **d, f, g**, and 50 μ m for **e**.

Figure 4 Wireless activation of ChR2 expressed in nociceptive pathways results in spontaneous pain behaviors and place aversion. **(a)** Representation of nociceptive pathways and illumination of nociceptive fibers with a sciatic LED stimulator. **(b)** Implantation of the sciatic LED stimulator has no effect on motor behavior vs. sham animals in the rotarod test ($P = 0.894$, $n = 5$ sham, $n = 8$ device). **(c)** Wireless activation of the sciatic LED stimulator causes increased nocifensive behaviors (flinching, hind paw licking, jumping) in Advillin-ChR2 mice but not in controls (17.5 vs. 1.2 flinches, $P < 0.0001$ vs. without illumination $n = 3$ per group). No other statistical comparisons reach significance. **(d)** Mice in a modified Y-maze. One arm is targeted with the RF antenna to operate the LED device (LED ON) and the other is not (LED OFF). Time spent in the center area (dashed lines) is not scored. **(e)** Heat maps from individual mice representing the time spent in each zone, red indicating more and blue indicating less time. In animals implanted with the sciatic LED device, aversion to the LED-ON zone is observed in TrpV1-ChR2 and Advillin-ChR2 mice, but not in controls. **(f)** Quantification of time spent in each zone of the Y-maze. TrpV1-ChR2 (420.5 vs. 644.5 s; $P = 0.011$, $n = 5$) and Advillin-ChR2 (491.2 vs. 656 s; $P = 0.001$, $n = 8$) mice display aversion to the LED-ON zone vs. the LED-OFF zone. No difference is observed in control mice (547.0 vs. 512.1 s; $P = 0.551$, $n = 10$). **(g)** Representation of ascending nociceptive pathways and illumination of primary afferent terminals innervating the spinal cord with a wireless epidural implant. **(h)** Wireless activation of the epidural LED implant increased nocifensive behaviors in SNS-ChR2 mice (64.2% vs. 0% of time; $P < 0.001$, $n = 3$). **(i)** Heat maps representing the time spent in each zone of the Y-maze. Red indicates areas where the animals spend a higher proportion of their time. Aversion to the LED-ON zone is observed in SNS-ChR2 mice but not in controls. **(j)** Quantification of the time spent in each zone of the Y-maze. SNS-ChR2 mice display aversion to the LED-ON zone (73 vs. 251 s; $P = 0.006$, $n = 3$). No difference is observed in control mice ($n = 3$). Group data are presented as mean \pm s.e.m. Statistical comparisons were made using two-tailed t -tests, except for **b**, which was a two-way ANOVA. * $P < 0.05$, ** $P < 0.01$.



volume of the cage, and was capable of activating multiple devices in the same region (Fig. 2g). These devices could be activated reliably up to 20 cm from the transmitters, which is ten times the reported range of any previous systems^{8–11} (Supplementary Fig. 10). Under these conditions, we calculated distributions of the specific absorption rate (SAR; a measure of the rate at which RF energy is absorbed by the body) and found that the SAR fell well below safety guidelines¹³ (Fig. 2f). This configuration allowed consistent device activation even with rapid changes in receiver location and orientation (Fig. 2h–j). This is demonstrated using long-exposure images captured during motion of an operating device; continuous streaks of light illustrate activation of the devices regardless of device position or orientation (Fig. 2i–j). (See Supplementary Notes 4 and 5 and Supplementary Figs. 10–12 for further discussion of the transmission efficiency with moving animals.)

To determine the utility of these optoelectronic devices in studies of pain pathways, we tested whether they could modulate pain-related behaviors of mice expressing ChR2 in all sensory neurons or in subpopulations of sensory neurons responsible for detection of noxious stimuli (nociceptors) (see Supplementary Note 6 and Online Methods). Mice expressing ChR2 in all sensory neurons were generated using a cre recombinase-based transgenic approach where cre recombinase expression is driven by the promoter of the sensory neuron-specific gene Advillin (Advillin-ChR2; Fig. 3a)^{14,15}. Electrophysiological studies show that Advillin-ChR2 sensory neurons were consistently activated by blue light (Fig. 3b,c and Supplementary Note 7), and immunohistochemical studies demonstrate that ChR2 was present in mid-axon, in the dorsal root ganglia (DRG) and in the central terminals of sensory neurons (Fig. 3d–f and Supplementary Note 8). Similar results were observed in mouse lines where ChR2 expression is restricted to nociceptor

populations (TrpV1-ChR2, SNS-ChR2; Supplementary Notes 6–8, Supplementary Figs. 13–17 and Supplementary Table 2).

Previous studies have shown that illumination of peripheral nerve terminals using an external light source on the skin induces spontaneous pain behaviors and place aversion in mice expressing ChR2 in sensory neurons^{1,3}. For these implantable devices to be viable for *in vivo* pain studies, illumination of ChR2-expressing axons (Fig. 4a) must generate action potentials. Consistent with this hypothesis, fiber-optic laser illumination of the exposed sciatic nerve in TrpV1-ChR2 mice produced reflexive withdrawal behaviors (Supplementary Fig. 18). It is also critical that device implantation not induce nerve injury or impair function. Devices implanted over the sciatic nerve for 2 weeks produced no signs of injury and no infiltration of immune cells compared to the contralateral nerve (Supplementary Figs. 19 and 20), and produced no motor impairment, even when the mouse was running (Supplementary Movie 1). This was quantified using the accelerating rotarod and open field tests, both of which indicated that the devices did not alter balance, motor coordination or locomotor activity compared with sham controls (Fig. 4b and Supplementary Fig. 21).

Devices implanted over the sciatic nerve in Advillin-ChR2 mice generated robust nocifensive responses. Wireless powering (20 Hz, 2.34 GHz RF, 3–5 dBm) of these devices produced reversible nocifensive behaviors in Advillin-ChR2 mice, but not in cre-negative littermates (Fig. 4c). These spontaneous responses are consistent with nociceptor activation. To evaluate whether optogenetic peripheral neuron activation produced behavioral aversion consistent with the perception of ongoing pain (as opposed to representing reflex activation), we placed mice in a modified Y-maze apparatus where one arm was exposed to a curtained RF (LED-ON) and one arm (LED-OFF) was not (Fig. 4d). Pretesting of devices in this arena demonstrated that activation occurred only in the LED-ON arm. Advillin-ChR2 mice showed significant aversion to the LED-ON arm compared to the LED-OFF arm (Fig. 4e,f), whereas cre-negative littermates spent a similar amount of time in the two arms. Similarly, TrpV1-ChR2 mice, which express ChR2 only in nociceptors, demonstrated significant aversion to the LED-ON arm compared to the LED-OFF arm (Fig. 4e,f).

With the epidural devices, we demonstrate optogenetic modulation of the spinal terminals of peripheral nerves using LED devices that are inserted in the epidural space (Fig. 4g). Implantation of devices into the epidural space did not cause significant damage to the spinal cord, as demonstrated histologically (Supplementary Fig. 22). Epidural device implantation also produced no impairment in motor behavior, locomotion or coordination compared to sham controls in the accelerating rotarod and open field tests (Supplementary Fig. 21). Activation of these devices (20 Hz, 2.24 GHz RF, 3–5 dBm) in the epidural space of SNS-ChR2 mice generated robust and reversible nocifensive behaviors that was entirely absent in cre-negative littermates (Fig. 4h). A Y-Arm maze assay to quantify behavioral aversion using SNS-ChR2 mice with epidural implants showed these mice had robust aversion to the LED-ON arm compared to littermate cre-negative mice (Fig. 4i–j).

These miniaturized, fully implantable, thin and soft optoelectronic systems enable robust operation and large transmission range without the need for optimization around specific cages or animal body types. The platforms are thinner by a factor of 5, more stretchable by a factor of 10, softer by a factor of 10,000 and more flexible by a factor of 10,000,000 than alternative technologies, thereby providing unique features in a wide variety of optogenetic applications. The low modulus of these biocompatible devices permits experiments in more extensive regions of the body and in a chronic manner, bypassing constraints associated with the hard mechanics and thick volumetric layouts of the most recently reported fully implantable designs¹⁰.

Providing easy access to this technology to the broader scientific community is essential to facilitate improved studies of neuronal circuitry. Our devices can be fabricated with 10 h of effort in standard laboratory facilities using inexpensive commercially available components, and the external power transmission systems require less than 1 h of training, making it possible for independent laboratories to construct and operate their own variants. Whereas the hand-crafted approach to device fabrication needed for other approaches¹⁰ offers some advantage in customization, it has limited potential to take advantage of increasingly powerful manufacturing approaches and accelerating trends in size miniaturization that drive progress in conventional optoelectronics. In contrast, our fabrication process is compatible with established flexible printed circuit board technologies and manufacturing tools from the electronics industry, making it possible to construct large numbers of devices in a cost-effective manner.

Extension of our approach to multiple LEDs could enable optogenetic modulation of the whole brain or other whole organs. Laminated

films with high thermal conductivity could improve the efficiency of heat dissipation, and optical diffusers could yield spatially uniform illumination. These advanced forms, as well as the present designs, have potential not only for basic research, but also as clinical tools. Gene therapy that could be used to deliver optogenetic channels to human cells is already in clinical trials^{16–20}, and with the appropriate testing these optogenetic stimulators could be adapted for use in treating chronic intractable human conditions such as chronic pain.

METHODS

Methods and any associated references are available in the [online version of the paper](#).

Note: Any Supplementary Information and Source Data files are available in the online version of the paper.

ACKNOWLEDGMENTS

This work was supported by a US National Institutes of Health (NIH) Director's Transformative Research Award (NS081707) to R.W.G., J.A.R. and M.R.B. D.S.B. was supported by an NIH Ruth L. Kirschstein F31 Predoctoral Fellowship (1F31NS078852). C.D.M. was supported by a Howard Hughes Medical Institute (HHMI) Medical Research Fellowship. B.A.C. was supported by a W.M. Keck Fellowship in Molecular Medicine and TR32 GM108539. M.Y.P. was supported by T32 GM007067. S.D. was supported by NS076324. Illustrations created by J. Sinn-Hanlon and P. Focken, University of Illinois. The authors appreciate the gifts of heterozygous SNS-cre mice from R. Kuner (University of Heidelberg), heterozygous TrpV1-cre mice from M. Hoon (NIH/National Institute of Dental and Craniofacial Research) and heterozygous Advillin-cre mice from F. Wang (Duke University). We would also like to thank R.E. Schmidt for the expertise he provided in neuropathological examination of tissue.

AUTHOR CONTRIBUTIONS

S.I.P. designed wireless optoelectronic systems, fabricated devices, tested devices, made wireless measurements, conducted simulations of wireless performance, designed experiments, generated figures, wrote and edited the manuscript. D.S.B. designed sciatic nerve devices, implanted devices, tested mice behavior, designed experiments, performed immunostaining, generated figures, wrote and edited the manuscript. G.S. designed and fabricated spinal cord devices, tested devices, generated figures, wrote and edited the manuscript. C.D.M. designed spinal cord devices, implanted devices, tested mice in behavior, designed experiments, performed immunostaining, generated figures, wrote and edited the manuscript. B.A.C. performed immunostaining and quantification, electrophysiology experiments, generated figures. H.U.C. and K.N.N. fabricated devices and tested devices. M.Y.P. performed surgical procedures, behavioral studies and electrophysiology, generated figures and edited the manuscript. S.D. performed experiments, implanted devices, generated figures. S.J.O., J.Y. and K.-I.J. made contributions to fabrication and testing of devices. V.K.S. performed experiments, immunostaining and generated figures. M.N. performed immunostaining and quantification of slides, as well as mouse breeding. J.G.G.-R. performed experiments and generated figures. S.K.V. performed immunostaining and mouse breeding. S.S.S. performed immunostaining and mouse breeding. K.M.W. performed immunostaining. J.S.H. made contributions to fabrication and testing of devices. R.X., T.P. and Y.H. performed mechanical simulations of device tolerance levels. T.K. designed and tested wireless optoelectronic systems for sciatic nerve. M.C.M. designed experiments and generated figures. J.P.G. performed immunostaining, generated figures, performed behavioral experiments, helped develop epidural implants and edited the manuscript. M.R.B. designed experiments. R.W.G. and J.A.R. oversaw all experiments and data analysis, designed experiments and devices, wrote and edited the manuscript.

COMPETING FINANCIAL INTERESTS

The authors declare no competing financial interests.

Reprints and permissions information is available online at <http://www.nature.com/reprints/index.html>.

- Iyer, S.M. *et al.* Virally mediated optogenetic excitation and inhibition of pain in freely moving nontransgenic mice. *Nat. Biotechnol.* **32**, 274–278 (2014).
- Towne, C., Montgomery, K.L., Iyer, S.M., Deisseroth, K. & Delp, S.L. Optogenetic control of targeted peripheral axons in freely moving animals. *PLoS One* **8**, e72691 (2013).
- Daou, I. *et al.* Remote optogenetic activation and sensitization of pain pathways in freely moving mice. *J. Neurosci.* **33**, 18631–18640 (2013).

4. Kozai, T.D. *et al.* Ultrasmall implantable composite microelectrodes with bioactive surfaces for chronic neural interfaces. *Nat. Mater.* **11**, 1065–1073 (2012).
5. Sparta, D.R. *et al.* Construction of implantable optical fibers for long-term optogenetic manipulation of neural circuits. *Nat. Protoc.* **7**, 12–23 (2012).
6. Jang, K.I. *et al.* Rugged and breathable forms of stretchable electronics with adherent composite substrates for transcutaneous monitoring. *Nat. Commun.* **5**, 4779 (2014).
7. Kim, D.H. *et al.* Epidermal electronics. *Science* **333**, 838–843 (2011).
8. Kim, T.I. *et al.* Injectable, cellular-scale optoelectronics with applications for wireless optogenetics. *Science* **340**, 211–216 (2013).
9. Xu, S. *et al.* Soft microfluidic assemblies of sensors, circuits, and radios for the skin. *Science* **344**, 70–74 (2014).
10. Montgomery, K.L. *et al.* Wirelessly powered, fully internal optogenetics for brain, spinal and peripheral circuits in mice. *Nat. Methods* **12**, 969–974 (2015).
11. Folcher, M. *et al.* Mind-controlled transgene expression by a wireless-powered optogenetic designer cell implant. *Nat. Commun.* **5**, 5392 (2014).
12. Harrington, R.F. *Time-Harmonic Electromagnetic Fields* (Wiley-IEEE Press, 2001).
13. IEEE Standard for Safety Levels with Respect to Human Exposure to Radio Frequency Electromagnetic Fields, 3 kHz to 300 GHz, IEEE Standard C95.1-2005 (Institute of Electronic and Electrical Engineers, 2005).
14. da Silva, S. *et al.* Proper formation of whisker barrelettes requires periphery-derived Smad4-dependent TGF-beta signaling. *Proc. Natl. Acad. Sci. USA* **108**, 3395–3400 (2011).
15. Hasegawa, H., Abbott, S., Han, B.X., Qi, Y. & Wang, F. Analyzing somatosensory axon projections with the sensory neuron-specific Advillin gene. *J. Neurosci.* **27**, 14404–14414 (2007).
16. Fink, D.J. *et al.* Gene therapy for pain: results of a phase I clinical trial. *Ann. Neurol.* **70**, 207–212 (2011).
17. Fink, D.J. & Wolfe, D. Gene therapy for pain: a perspective. *Pain Manag.* **1**, 379–381 (2011).
18. Miyazato, M. *et al.* Suppression of detrusor-sphincter dyssynergia by herpes simplex virus vector mediated gene delivery of glutamic acid decarboxylase in spinal cord injured rats. *J. Urol.* **184**, 1204–1210 (2010).
19. Yokoyama, H. *et al.* Gene therapy for bladder overactivity and nociception with herpes simplex virus vectors expressing preproenkephalin. *Hum. Gene Ther.* **20**, 63–71 (2009).
20. Pleticha, J. *et al.* Preclinical toxicity evaluation of AAV for pain: evidence from human AAV studies and from the pharmacology of analgesic drugs. *Mol. Pain* **10**, 54 (2014).

ONLINE METHODS

For all mouse studies, institutionally approved protocols were followed for all aspects of this study.

Device design and fabrication. The harvesting unit receives signals from a transmitter, rectifies them, multiplies the voltages (3x) and routes the resulting direct-current output to the LEDs. The harvesting unit is an impedance matching circuit consisting of a ceramic chip capacitor (1 pF; 0.20 mm width, 0.4 mm length, 0.22 mm thickness; bonded by solder paste) and an inductor (2.7 nH; 0.20 mm width, 0.4 mm length, 0.22 mm thickness; bonded by solder paste) connected in series. The rectifier uses miniaturized Schottky diodes (1.7 mm width, 1.5 mm length, 0.5 mm thickness) and ceramic chip capacitors (5 pF; 0.20 mm width, 0.4 mm length, 0.22 mm thickness; bonded by solder paste). The multiplier includes three Schottky diodes identical to those in the rectifier, and boosts voltages provided by the rectifier (~0.9 V) to values sufficient to operate the LEDs (~2.7 V; 220 μ m width, 270 μ m length, and 50 μ m thickness for spinal device; 1.6 mm length, 0.8 mm width, and 0.75 mm for peripheral devices).

Fabrication begins with a clean glass slide (75 mm long, 50 mm width, and 1 mm thickness), with a layer (200 nm thickness) of polymethyl methacrylate (PMMA, 495 PMMA A6, Microchem) and a 2 μ m layer of polyimide (PI) formed by spin-casting at 3000 rpm for 60 s, cured at 250 °C for 2 h. Photolithography (AZ 4620, AZ Electronic Materials) defines the necessary conducting traces after e-beam deposition of Ti/Au (3 μ m thickness). A second 2 μ m PI layer serves as encapsulation for making a mechanically neutral plane. Photolithography and reactive ion etching then define the PI/metal/PI layers into serpentine-shaped structures. The LED and circuit chips are placed onto the exposed pads (**Supplementary Fig. 1**) with a small amount (5–20 particles) of solder paste (SMD290SNL250T5, Chipquik). The substrate is then cured at 250 °C in a vacuum oven for 10 min to electrically bond the LEDs and the surface-mounted device components to the conductive traces. An encapsulating layer of polydimethylsiloxane (PDMS), spin-cast and cured at 70 °C for 1 h seals the device before its release from the substrate by dissolution of the PMMA in acetone. For the epidural device, the narrow serpentine area (~360 μ m width) and LED are inserted into a Teflon tube (PTFE-28-25, SAI), with an inner diameter of 380 μ m. PDMS is added to the tube. The devices is cast and cured in the tube, which is then removed to complete the fabrication. The timing and steps required for device fabrication are detailed in **Supplementary Note 1**.

Configuration: RF system for power transmission. The RF transmission system consists of a signal generator (N5181 MXF, Agilent), a power amplifier (1189/BBM3K5KKO, Richardson RFPD), a DC power supply (U8031A, Keysight Technologies) with a heat sink (53M7972, Fischer Elektronik), and TX antennas (PE51019-3, Pasternack Enterprises) with a splitter (RFLT4W0727GN, RFLambda). The amplifier and the fan are powered by separate DC power supplies. The outputs (channels 1 & 2) connect to the J3 input of the amplifier, with VDD into Pins #6, 7 and GND into Pins #8, 9 and to the fan, respectively. The output of the signal generator connects to the input of the amplifier, which is connected to the splitter to output to all of the TX antennas.

Animals and genetic strategy. Adult mice (8–12 weeks of age) are used for this study. Mice are housed in the animal facilities of the Washington University School of Medicine on a 12 h light/dark cycle, with access *ad libitum* to food and water. Institutionally approved protocols are followed for all aspects of this study.

Three cre-driver lines were used for this study including heterozygous SNS-cre mice from Rohini Kuner²¹, heterozygous TrpV1-cre mice from Mark Hoon²², and heterozygous Advillin-cre mice provided by Fan Wang¹⁴. Mice from each of these three lines were crossed to homozygous Ai32 mice from Jackson Laboratory. As previously described, Ai32 mice harbor ChR2 (H134R)-eYFP in the Gt(ROSA)26Sor locus²³. To generate mice with conditional expression of ChR2 in specific populations of sensory neurons, mice with ChR2 in the Rosa locus (Ai32 mice) were crossed to mice expressing cre from various sensory neuron-specific driver gene loci (Advillin, TrpV1, or SNS). For the purposes of this study, the three lines generated were referred to as Advillin-ChR2, TrpV1-ChR2 and SNS-ChR2, respectively.

Surgical procedure: sciatic device implantation. The surgical procedure was modified from the Chronic Constriction Injury procedure²⁴. Mice were anesthetized with isoflurane and their eyes were covered with Altalube ointment (Altaire Pharmaceuticals, Riverhead, NY) to prevent corneal drying. A small skin incision was made over the greater trochanter of the femur on the left flank of the animals. The fascia connecting the biceps femoris and the gluteus maximus was bluntly dissected apart to open a plane between the muscles, in which the sciatic nerve was clearly accessible. The fascia connecting the underlying muscle in the area directly rostral to the incision was bluntly dissected apart using needle driver forceps. The body of the device was inserted under the skin into the subcutaneous pocket generated by the blunt dissection. The gluteus maximus was pulled caudally to expose the sciatic nerve, and the tip of the device containing the LED was folded under the gluteus and placed over the nerve. The gluteus maximus was pulled over the device and sutured into place with a resorbable Ethicon 6-0 vicryl suture (Cornelia, GA) to restore the original muscle architecture, and to secure the device between the muscles and above the nerve. The left flank incision was sutured closed using Ethicon 6-0 nylon monofilament suture and the mouse was allowed to recover from anesthesia in a warmed chamber.

Surgical procedure: epidural device implantation. Under isoflurane anesthesia on an isothermal heating pad, a 2-cm midline incision was made on the back, exposing the thoracolumbar vertebral transition. The paraspinous muscles were separated, exposing the T13 spinous process and lamina. A partial laminectomy was made at the rostral end of this landmark level, allowing insertion of the epidural stimulator with the LEDs centered over the dorsal horn of the L4-L6 spinal cord segment²⁵. The distal end of the epidural stimulator and proximal stretchable antenna were secured with 6-0 suture. The skin was closed using interrupted sutures and mice were allowed to recover on an isothermal pad with access to food and water *ad libitum*.

Surgical procedure: spinal nerve ligation (SNL). Mice were deeply anesthetized with vaporized isoflurane, and the paraspinous muscles were bluntly dissected to expose the L5 transverse process. The L5 process was removed, the L4 spinal nerve was tightly ligated with silk suture (6-0, Ethicon; Cornelia, GA) and the nerve was transected distal to the ligation. The skin was closed with staples and the animal was allowed to recover on an isothermal heating pad.

Surgical procedure: chronic constriction injury (CCI). The procedure was performed as described previously²⁴. In brief, mice were deeply anesthetized with vaporized isoflurane and a small incision was made over the left flank. The fascial layer between the biceps femoris and gluteus maximus was bluntly dissected to expose the sciatic nerve. Two loose chromic gut sutures were tied around the nerve, which was then resected and the muscular architecture was re-approximated on top of it. The skin was closed with interrupted sutures, and the animal as allowed to recover on an isothermal heating pad.

Direct laser activation of the sciatic nerve in an open preparation. Mice were anesthetized with 2% isoflurane. A small skin incision was made over the greater trochanter of the femur on the left flank of the animals. The fascia connecting the biceps femoris and the gluteus maximus was bluntly dissected apart to open a plane between the muscles, in which the sciatic nerve was clearly accessible. A small cutaneous incision over the lateral leg of the mouse was made, and two silver electrodes were implanted in the exposed quadriceps muscles to amplify and record electrical activity representing muscle response. After completion of the surgical preparation, the isoflurane anesthesia was gradually reduced over 2 h to ~0.875% until a flexion reflex response (evoked by pinching the paw) was present but spontaneous escape behavior and righting reflex were still absent. The animals were not restrained in any fashion. Body temperature was maintained using an overhead radiant light and monitored throughout the experiment. These conditions were optimized to establish a stable depth of anesthesia and consistent baseline sciatic muscular activity. A laser stimulus delivered through a fiber-optic cable was then used to stimulate the sciatic nerve while the EMG response was recorded in real-time using a Grass CP511 preamplifier connected to a PC via a WinDaq DI-720 module. The data were exported for analysis to Igor Pro 6.05 software (Wavemetrics, Portland, OR). Using a custom script, the EMG signals were

subtracted from the baseline, rectified and integrated to quantify the area under the curve. The area under the curve for the motor response was presented in arbitrary units. The investigator quantifying the motor response was blinded to testing condition.

Behavioral analyses. For behavioral studies, a priori power analyses were performed to estimate necessary sample sizes. However, study results demonstrated effect magnitudes larger than anticipated, and therefore, increased animal numbers could not be justified. For all behavioral analyses, the experimenters were blind to genotype and treatment (implant vs. sham). Animals from each genotype were randomly selected for implant vs. sham.

Behavior: spontaneous behavior. Each mouse was placed in an individual plexiglass behavioral chamber. Mice were allowed to acclimate for at least 30 min before testing in the presence of white noise generators to reduce the influence of external noise pollution on testing. To measure spontaneous behaviors, the wireless LED devices were activated using the RF signal generator antenna at 3–5 dBm and 2.0–2.5 GHz. Behavior was recorded through an HD video camera (Sony) for one minute. Nocifensive behaviors (defined as licking hind paws, vocalizations, or jumping) were quantified post-hoc from the video recordings while blinded to genotype.

Behavior: Y-maze. Place aversion was tested in two arms of a Y-maze constructed of plexiglass with a layer of corn cob bedding. Each arm of the maze was 10 cm wide × 100 cm long and was marked with either vertical or horizontal black stripes with a neutral area between the arms. To generate the RF signal, one antenna was located below an arm of the maze allowing for the control of LED devices through the maze floor and a second antenna was positioned on the side of the same arm to ensure complete local field coverage. To begin the experimental protocol, a mouse was placed in the neutral area of the maze and was continuously monitored and recorded through a video connection for 20 min. During this time an experimenter blinded to the genotype manually controlled the RF signal by watching the monitoring system. Upon entry of the mouse into the “ON” chamber, activation of the LED device through the RF antenna was initiated; likewise, upon departure from the “ON” chamber RF activation was terminated. Video data were collected and time-in-chamber was analyzed using Ethovision software (Noldus, Leesburg, VA.).

Behavior: Rotarod. The method for this technique has been described previously^{27,28}. Briefly, an accelerating Rotarod (Ugo Basile) was used to study motor coordination and balance after implantation of the epidural and sciatic stimulators. Five consecutive acceleration trials were performed with 5 min breaks separating each acceleration trial.

Behavior: open field. As described previously, locomotion was measured in a Versamax Animal Activity Monitoring System (AccuScan Instruments) Open Field Arena^{26,27}. Mice were initially habituated to the climate-controlled test room for 1 h before testing. Locomotor activity was assessed by recording beam breaks in this 42 (length) × 42 (width) × 30 (height) cm chamber for 1 h. The total distance traveled during this time, time spent moving, and the number of horizontal beam breaks was calculated for the entire chamber.

DRG culture. Lumbar DRG were dissected from 6- to 8-week old Advillin-ChR2, TrpV1-ChR2 or SNS-ChR2 mice in HBSS + 10 mM HEPES on ice and digested in 45U papain (Worthington Biochemical) in HBSS+H for 20 min at 37 °C. The tissue was washed with HBSS+H and then further digested in collagenase (1.5 mg/ml; Sigma) for an additional 20 min at 37 °C. After washing, cells were dissociated in Neurobasal A media (Gibco) containing 5% FBS (Life Technologies), 1× B27 supplement (Gibco), 2 mM GlutaMAX (Life Technologies) and 100 U/ml penicillin/streptomycin (Life Technologies). The tissue suspension was then filtered using a 40 μm nylon cell strainer, and centrifuged at 1,000g for 3 min, resuspended, triturated and then centrifuged at 1,000g. Neurons are resuspended in DRG media and plated onto coverslips coated with collagen and poly-D-lysine (Sigma). Cells were cultured for 3–4 days before electrophysiology experiments.

Electrophysiology. Whole-cell patch clamp recordings were made from cultured DRG neurons using pipettes with resistance values ranging from 2–3 megaohms, filled with (in mM) 120 potassium gluconate, 5 NaCl, 2 MgCl₂, 0.1 CaCl₂, 10 HEPES, 1.1 EGTA, 4 Na₂ATP, 0.4 Na₂GTP, 15 sodium phospho-creatine; pH adjusted to 7.3 using KOH, osmolarity 291 mOsm. The extracellular solution consists of (in mM): 145 NaCl, 3 KCl, 2 CaCl₂, 1.2 MgCl₂, 10 HEPES, 7 glucose; pH adjusted to 7.3 with NaOH. Recordings and light stimulation were performed using Patchmaster software (HEKA Instruments, Bellmore, NY) controlling an EPC10 amplifier (HEKA Instruments). Neurons were voltage clamped at –60 mV and held at –60 mV for current clamp recording. Optical stimulation was delivered with collimated light through the microscope objective, using a custom set-up with a blue LED (M470L2; Thorlabs) coupled to the back fluorescent port of an Olympus BX-51 microscope. Light intensity at the focal plane (10 mW/mm²) was calculated using a photodiode (S120C, Thorlabs) and power meter (PM100D, Thorlabs).

Immunohistochemistry. Mice were deeply anesthetized with a ketamine, xylazine and acepromazine cocktail, then transcardially perfused with cold 4% paraformaldehyde in PBS. Lumbar DRG, spinal cord and sciatic nerves were dissected and placed in 30% sucrose in PBS for overnight cryoprotection, then frozen in OCT. Frozen tissue was then sectioned in a –20 °C cryostat (Leica) at either 30 μm (spinal cord and cross section sciatic nerve), 18 μm (DRG), or 6 μm (longitudinal sciatic nerve) and collected directly onto frosted glass slides. Immunohistochemistry was conducted as described previously²⁸. Goat anti-CGRP (1:400, AbD Serotec Cat# 1720-9007), rabbit anti-GFP (1:1,000, Life Technologies Cat# A11122), mouse anti-NF200 (1:400, Millipore Cat# MAB5266), mouse anti-GFAP (1:500, Cell Signaling Technologies), rabbit anti-Iba1 (1:300, Wako Biochemicals cat# 019-19741), goat anti-choline acetyltransferase (1:100, EMD Millipore cat# AB144P) and mouse anti-βIII-tubulin (1:1,000, Covance Research Products Inc. Cat# PRB-435P-100) were used whereas IB4⁺ labeling was performed using an Alexa Fluor 568-conjugated IB4 (1:400, Life Technologies Cat #I21412). Research Resource IDs were provided below to assist the reader. Fluorescent-conjugated secondary antibodies (Life Technologies) were used to visualize primary immunostaining: donkey anti-goat AF647 (1:500), donkey anti-rabbit AF488 (1:500), and goat anti-mouse AF647 (1:500). Slides were sealed overnight with Prolong Gold Antifade Mountant with DAPI (Life Technologies). Images from sealed slides were obtained using a Leica SPE confocal microscope, with gain and exposure time constant throughout image groups.

Antibody, dilution, company, catalog ID, research resource ID. Goat anti-CGRP, 1:400, AbD Serotec, 1720-9007, AB_2290729. Rabbit anti-GFP, 1:1,000, Life Technologies, A11122, AB_22156. Rabbit Anti-Iba1, 1:300, Wako Chemicals, 019-19741, AB-839504. Mouse anti-NF200, 1:400, Sigma-Aldrich, N0142, AB_2149763. Mouse anti-βIII-tubulin, 1:1,000, EMD Millipore, 05-166, AB_291637. Goat anti-ChAT, 1:100, EMD Millipore, AB144P, AB_11214092. Guinea Pig anti-GFAP, 1:500, Synaptic Systems, 173-004, AB_10641162. Mouse anti-GFAP, 1:500, Cell Signaling Technologies, 3670, AB_561049.

- Agarwal, N., Offermanns, S. & Kuner, R. Conditional gene deletion in primary nociceptive neurons of trigeminal ganglia and dorsal root ganglia. *Genesis* **38**, 122–129 (2004).
- Mishra, S.K., Tisel, S.M., Orestes, P., Bhangoo, S.K. & Hoon, M.A. TRPV1-lineage neurons are required for thermal sensation. *EMBO J.* **30**, 582–593 (2011).
- Madisen, L. *et al.* A toolbox of Cre-dependent optogenetic transgenic mice for light-induced activation and silencing. *Nat. Neurosci.* **15**, 793–802 (2012).
- Bennett, G.J. & Xie, Y.K. A peripheral mononeuropathy in rat that produces disorders of pain sensation like those seen in man. *Pain* **33**, 87–107 (1988).
- Harrison, M. *et al.* Vertebral landmarks for the identification of spinal cord segments in the mouse. *Neuroimage* **68**, 22–29 (2013).
- Golden, J.P. *et al.* Dopamine-dependent compensation maintains motor behavior in mice with developmental ablation of dopaminergic neurons. *J. Neurosci.* **33**, 17095–17107 (2013).
- Montana, M.C. *et al.* The metabotropic glutamate receptor subtype 5 antagonist fenobam is analgesic and has improved *in vivo* selectivity compared with the prototypical antagonist 2-methyl-6-(phenylethynyl)-pyridine. *J. Pharmacol. Exp. Ther.* **330**, 834–843 (2009).
- Golden, J.P. *et al.* RET signaling is required for survival and normal function of nonpeptidergic nociceptors. *J. Neurosci.* **30**, 3983–3994 (2010).

Supplementary Note 1: System layouts and characteristics of LEDs

Supplementary Fig. 1 shows the circuit layouts of peripheral (**Supplementary Fig. 1a**; top) and spinal epidural devices (**Supplementary Fig. 1b**; top), and the respective component information (**Supplementary Fig. 1a-b**; bottom). The harvesting unit is an impedance matching circuit consisting of a ceramic chip capacitor (1 pF; 0.20 mm width, 0.4 mm length, 0.22 mm thickness; bonded by solder paste) and an inductor (2.7 nH; 0.20 mm width, 0.4 mm length, 0.22 mm thickness; bonded by solder paste) connected in series. The rectifier uses miniaturized Schottky diodes (1.7 mm width, 1.5 mm length, 0.5 mm thickness) and ceramic chip capacitors (5 pF; 0.20 mm width, 0.4 mm length, 0.22 mm thickness; bonded by solder paste). The multiplier includes three Schottky diodes identical to those in the rectifier, and boosts voltages provided by the rectifier (~0.9 V) to values sufficient to operate the LEDs (~2.7 V; 220 μm width, 270 μm length, and 50 μm thickness for spinal device; 1.6 mm length, 0.8 mm width, and 0.75 mm thickness for peripheral devices). Electrical characteristics of the LEDs appear in **Supplementary Fig. 2**. The built-in voltage is 2.7 V and the peak emission wavelengths are 470 nm (APT1608LVBC/D, Kingbright) and 465 nm (C460TR2227-0216, Cree Inc.) to match the absorption characteristics of channelrhodopsin (**Supplementary Fig. 2a**). The current-voltage (**Supplementary Fig. 2b**) and optical power density-current (**Supplementary Fig. 2c**) graphs shows a current of 0.6 mA at 2.7 V, and output power density of ~10 mW/mm² at 0.6 mA. The LED has a radiation angle of 120°.

The stress-strain curves of the PDMS layer and the full system were measured with the Q800-Dynamic Mechanical Analysis (DMA) system (TA Instruments) (**Supplementary Fig. 3**). Both samples were prepared with dimensions of 20 mm length, 10 mm width, and 0.5 mm thickness. The elastic Young's modulus is ~0.5 MPa for the PDMS alone with stretching up to 100 %, and ~1.7 MPa for the full device with stretching up to 40 % before operation failure occurred.

Supplementary Note 2: Center frequencies dependency on hydration

For antennae implanted in biological tissues, one thing that can impact the center frequency of the antenna is hydration status. In order to assess how hydration affects antenna function, we performed simulations. In these calculations, we used the Cole-cole relaxation dielectric model below and parameters for dry and wet skin described in the reference section.^{1,2}

$$\varepsilon_r(\omega) = \varepsilon_\infty + \sum_n \frac{\Delta\varepsilon_n}{1 + (i\omega\tau_n)^{1-\alpha_n}} + \frac{\delta_i}{i\omega\varepsilon_0}$$

where δ is conductivity, τ is the relaxation time constant, ε_0 is the static relative permittivity, and ε_r is the relative permittivity.

The wide bandwidth (200 MHz) of the stretchable antenna allows it to harvest RF power from a much wider range of transmitting frequencies than conventional patch antennae (bandwidth ~50 MHz) (**Supplementary Fig. 4d**). This characteristic reduces the likelihood that a mismatch between the receiver and transmitter will prevent device activation. Based on this model, if the center frequency of an antenna implanted in an animal shifts from 2.33 GHz to 2.25 GHz due to changing physiological conditions or strains, the patch antenna harvests less than 10 % as much power as it did before the shift, while the stretchable antenna still harvests more than 90 % (**Supplementary Fig. 4c**). This result suggests that the stretchable antenna can function efficiently in biological environments despite changes in the temperature or hydration of the surrounding materials, or the application of strain.

Simulation results reveal that the center frequency shifts toward lower frequencies when implanted under wet skin compared to dry skin (**Supplementary Fig. 5a**). This shift confirms that the electromagnetic characteristics of biological tissues depend on hydration condition, and that wet tissues are more dispersive than dry tissues. Mechanical simulations show how strain affects center frequencies under both wet and dry tissue (**Supplementary Fig. 5b**). While this simulation suggests that shifts in the center frequency can arise from strain underneath wet tissue, an antenna with a wide bandwidth center frequency can undergo these shifts and remain operational and efficient without changing the transmission wavelength.

Supplementary Note 3: Thermal measurements

We put the implantable devices inside hydrogel that has similar thermal properties to biological tissues. The devices and gel were warmed to 37 °C using a hot plate to simulate biological temperatures. The harvester was powered wirelessly and operated under the same conditions that

are used in behavior tests (10 mW/mm² optical output density, 20 Hz pulse and 10 ms duration for 10 mins). Variations in temperature due to device activation were monitored with ultrathin thermal sensors which were implanted at three different positions between the LED and the hydrogel (**Supplementary Fig. 9a**). Modeling data were used to compare the results for each temperature probe (**Supplementary Fig. 9b**). The results show transient heating at the LED surface that is correlated with pulsed operation of the LED (20 Hz, 10 ms duration). Transient but minute heating is also detected at the PDMS tube-hydrogel interface 190 μm away from the LED (**Supplementary Fig. 9c-e**). There were no noticeable variations (< 0.1 °C) of temperature when the sensor was 440 μm from the LED (**Supplementary Fig. 9c-e**).

Supplementary Note 4: TX efficiency for activation of peripheral nerve devices

Incident RF radiation and its coupling into a dynamically moving antenna are crucial to the utility of these devices. The efficiency of RF coupling can be described using the transmission coefficient (S_{12}), the optical power density, and the angular radiation patterns. All three of these parameters, which are calculated here using simulations, are necessary to fully describe the characteristics of RF harvesting with wireless devices.

S_{12} corresponds to the logarithm of the fraction of an electromagnetic wave that passes through a surface. A large S_{12} indicates efficient coupling between the TX and receiving systems (**Supplementary Fig. 11a**), but the S_{12} can vary with antenna positioning. In the case of devices implanted in freely-behaving animals, S_{12} varies with different activities such as walking, standing, or lying down. To assess the effect of this variation on device operation, the values of S_{12} for walking, standing, and lying were calculated and normalized to the value of S_{12} for walking. The S_{12} at a frequency of 2.34 GHz for walking, standing, and lying are 0, -0.42, and -0.93 (**Supplementary Fig. 11a**). This means that if the antenna receives 100 μW while the mouse is walking it would receive 89.5 μW and 98.2 μW if the mouse were instead standing on its hind legs or lying down. A reduction of received power by 10-20 % corresponds to a reduction of 3-6 % in simulated optical output power due to the conversion efficiency of the LEDs (30 %).

Calculations for S_{12} indicate the total optical power density available as a function of position across the cage. These levels lie within an acceptable range for optogenetic activation (**Supplementary Fig. 11b-d**; right). To supplement the simulations, measurements of optical power density along the bottom of a cage (**Supplementary Fig. 10a**) and maps of simulated optical power density as a function of the distance from the bottom of the cage were generated (**Supplementary Fig. 10b-g**). The results are consistent with the modeling data (**Supplementary Fig. 10h-l**). The power delivered to the device depends also on the orientation, as determined by the angular radiation patterns, which allow the calculation of the area of overlap between the TX antenna and the implantable antenna; increases in the overlap of radiation patterns associated with the TX antenna and the receiving antenna correspond to improved coupling.³ Walking and standing postures involve orientations that both yield ~33 % areas of overlap, due to similar radiation and coupling patterns (**Supplementary Fig. 11b-d**; middle). Somewhat reduced coupling (~27 % area of overlap) occurs in the lying posture due to loss of power associated with transmission through biological tissues (**Supplementary Fig. 11d**; middle). The results suggest that wireless activation of the sciatic nerve devices will be consistent and uniform for all mouse orientations and locations.

Supplementary Note 5: TX configuration for activation of spinal cord regions

The efficiency of RF coupling must also be assessed for the epidural devices (**Supplementary Fig. 12a**), in addition to the peripheral nerve devices described in **Supplementary Note 4**. S_{12} for the antenna used in the epidural devices at 2.24 GHz when the mice are walking, standing, or lying down is -0.68, -0.1, and 0 (**Supplementary Fig. 12b**). This result shows that if the antenna receives 91.6 μW while walking, it would receive of 99.2 μW and 100 μW if the mouse were instead standing on its hind legs or lying down. A reduction in the received power by 10-20 % corresponds to a reduction of 3-6 % in optical output power due to the conversion efficiency of LEDs (30 %). The conclusions based on S_{12} are reinforced by the angular radiation patterns of the antenna (**Supplementary Fig. 12c-e**; left). In these plots, increases in the overlap of radiation patterns associated with the TX antenna and the receiving antenna correspond to improved coupling. The lying and standing postures both yield ~33 % areas of overlap, because these cases involve orthogonal orientation to the TX antennas, with similar radiation and coupling patterns (**Supplementary Fig. 12d-e**; left). Somewhat reduced coupling (~29 % area of overlap) occurs

when walking due to loss of power associated with transmission through biological tissues (**Supplementary Fig. 12c**; left).^{4,5} Collectively, the S₁₂ and angular radiation patterns show that this transmission configuration allows uniform wireless activation of epidural devices within the targeted area regardless of mouse orientation or location (**Supplementary Fig. 12c-e**; right).

Supplementary Note 6: Generating the mouse lines for optogenetic studies

A transgenic cre-recombinase approach was used to generate mice with ChR2 expression limited to nociceptors by crossing heterozygous TrpV1-Cre mice with homozygous Ai32 mice, producing a TrpV1-ChR2 line (**Supplementary Fig. 13a**), or by crossing heterozygous SNS-Cre mice to Ai32 mice, producing a SNS-ChR2 line (**Supplementary Fig. 14a**). Details of these lines and crosses are provided in **Online Methods**.

Supplementary Note 7: Electrophysiological characterization of ChR2 expressing dorsal root ganglia neurons

Whole-cell patch clamp recordings from cultured dorsal root ganglia (DRG) neurons from adult Advillin-ChR2 mice demonstrate large inward photocurrents in response to blue light illumination (470 nm, 10 mW/mm²), confirming functional channel expression and trafficking in peripheral neurons (**Figure 3b**, bottom trace). Current-clamp recordings reveal persistent action potential firing in response to constant illumination in some neurons (**Figure 3b**, top trace), while in others only a single action potential is elicited at the onset of illumination. Similarly, we are able to drive firing with high fidelity using short pulses of light at defined frequencies up to 20 Hz in some cells (**Figure 3c**), but many cells fire at lower fidelity. Detailed electrophysiological characteristics of TrpV1-ChR2 dorsal root ganglion neurons can be found in **Supplementary Table 2**. These data and previous studies⁶ demonstrate that neuronal output in ChR2-expressing sensory neurons can be controlled using blue light. Similar data demonstrating the excitability of TrpV1-ChR2 or SNS-ChR2 neurons with light are included in **Supplementary Fig. 13b-c and 14b-c**.

Supplementary Note 8: Immunohistological characterization of ChR2 expression

Immunohistochemical analysis of adult Advillin-ChR2 mice confirms ChR2 expression along all axes of the peripheral nervous system. Centrally projecting axons expressing ChR2 are found

throughout the spinal cord dorsal horn (green, **Figure 3d**), including nociceptive fibers that terminate in lamina I and II where they are co-labeled with IB4 (non-peptidergic nociceptors, red) or CGRP (peptidergic nociceptors, purple). Staining of the dorsal root ganglion reveals ChR2 expression in most neurons, as confirmed by co-expression with the neuron-specific microtubule protein β III-tubulin (green and purple, **Figure 3e**). Additionally, all neurons that bind IB4 (red) express ChR2 (green, **Figure 3e**). We also confirmed that ChR2 was efficiently trafficked in peripherally-projecting axons. Longitudinal- (**Figure 3f**) and cross-sections (**Figure 3g**) of the sciatic nerve show robust ChR2 expression along the fibers, which is observed in a subset of myelinated axons marked by NF200 (purple).

Immunohistochemical analysis of adult Advillin-ChR2 mice confirms ChR2 expression in the dorsal root ganglion. There is significant overlap of ChR2-EYFP (green) expression with β III tubulin (purple) within the soma (**Supplementary Fig. 15a** 82 ± 3 %). There is also significant expression of ChR2-EYFP (green) within the subpopulation of non-peptidergic neurons, identified through labeling for IB4 (red) (**Supplementary Fig. 15b-c** 29 ± 6 %) and the subpopulation of peptidergic neurons, identified through labeling for CGRP (blue) (**Supplementary Fig. 15b-c** 57 ± 8 %).

Immunohistochemical analysis of adult TrpV1-ChR2 mice confirms ChR2 expression along all axes of the peripheral nervous system. Centrally projecting axons expressing ChR2 are found throughout the spinal cord dorsal horn (green, **Supplementary Fig. 13d**), including nociceptive fibers that terminate in lamina I and II where they are co-labeled with IB4 (non-peptidergic nociceptors, red) or CGRP (peptidergic nociceptors, purple). Staining of the dorsal root ganglion reveals ChR2 expression in many neurons, as confirmed by co-expression with the neuron-specific microtubule protein β III-tubulin (green and purple, **Supplementary Fig. 13e**). We also confirmed that ChR2 was efficiently trafficked in peripherally-projecting axons. Longitudinal- (**Supplementary Fig. 13f**) and cross-sections (**Supplementary Fig. 13g**) of the sciatic nerve show robust ChR2 expression along the fibers, which is observed in a subset of myelinated axons marked by NF200 (purple).

Immunohistochemical analysis of adult TrpV1-ChR2 mice confirms ChR2 expression in the

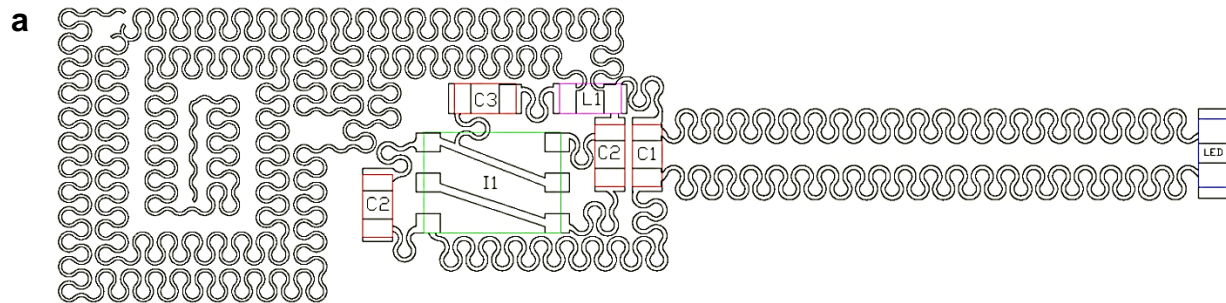
dorsal root ganglion. There is significant overlap of ChR2-EYFP (green) expression with β III tubulin (purple) within the soma (**Supplementary Fig. 16a** 59 ± 3 %). There is also significant expression of ChR2-EYFP (green) within the subpopulation of non-peptidergic neurons, identified through labeling for IB4 (red) (**Supplementary Fig. 16b-c** 41 ± 5 %) and the subpopulation of peptidergic neurons, identified through labeling for CGRP (blue) (**Supplementary Fig. 16b-c** 51 ± 7 %).

Immunohistochemical analysis of adult SNS-ChR2 mice confirms ChR2 expression along all axes of the peripheral nervous system. Centrally projecting axons expressing ChR2 are found throughout the spinal cord dorsal horn (green, **Supplementary Fig. 14d**), including nociceptive fibers that terminate in lamina I and II where they are co-labeled with IB4 (non-peptidergic nociceptors, red) or CGRP (peptidergic nociceptors, purple). Staining of the dorsal root ganglion reveals ChR2 expression in many neurons, as confirmed by co-expression with the neuron-specific microtubule protein β III-tubulin (green and purple, **Supplementary Fig. 14e**). We also confirmed that ChR2 was efficiently trafficked in peripherally-projecting axons. Longitudinal- (**Supplementary Fig. 14f**) and cross-sections (**Supplementary Fig. 14g**) of the sciatic nerve show robust ChR2 expression along the fibers, which is observed in a subset of myelinated axons marked by NF200 (purple).

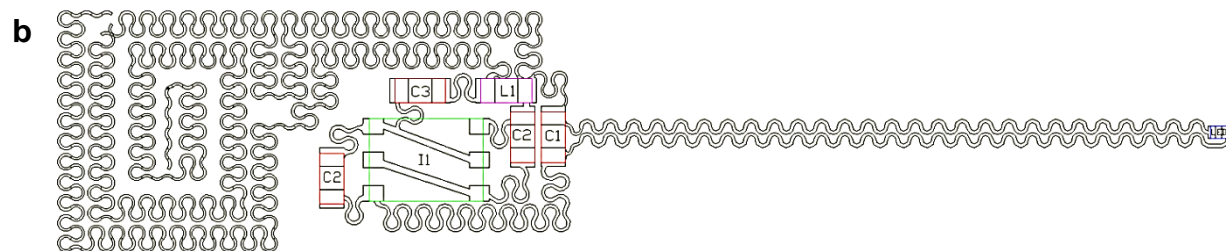
Immunohistochemical analysis of DRG neurons of adult SNS-ChR2 mice has been previously described in the literature. We also confirmed that ChR2 expression is absent in ventral horn motor neurons in all three mouse lines (**Supplementary Fig. 17**).

Reference

1. Park, S.-I. Enhancement of Wireless Power Transmission into Biological Tissues Using a High Surface Impedance Ground Plane. *PIER* **135**, 123-136 (2013).
2. Gabriel, S. The dielectric properties of biological tissues:III.Parametric models for the dielectric spectrum of tissues. *Phy. in Med. and Bio.* **41**,2271-2293 (1996).
3. Harrington, R.F. Time-Harmonic Electromagnetic Fields 2nd edn *Wiley-IEEE Press.* (2001).
4. Engineers, I.f.E.a.E., Vol. C95.1-2005 (2005).
5. Park, S.-I. et al. Ultraminiaturized photovoltaic and radio frequency powered optoelectronic systems for wireless optogenetics. *J.Neural Eng.* **12**, 056002 (2015).
6. Daou, I. et al. Remote optogenetic activation and sensitization of pain pathways in freely moving mice. *J. Neurosci* **33**, 18631-18640 (2013).



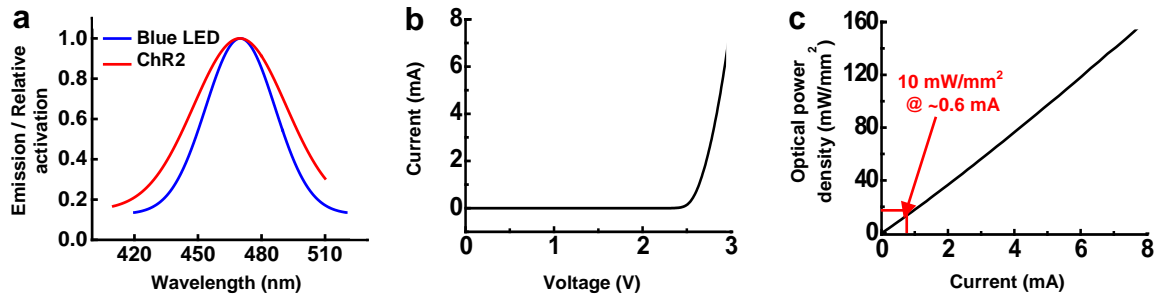
	Components	Product number	Vendor information
LED	470 nm, 1.6 mm x 0.8 mm x 0.7 mm	APT1608LVBC/D	Kingbright
C1,3	Capacitor, 1 pF, 0.2 mm x 0.4 mm x 0.22 mm	250R05L1R0BV4T	Johanson Technology
C2	Capacitor, 5 pF, 0.6 mm x 0.3 mm x 0.33 mm	250R05L5R1CV4T	Johanson Technology
I1	Schottky diode, 1.7 mm x 1.5 mm x 0.5 mm	1PS66SB82,115	NXP Semiconductor
L1	Inductor, 2.7 nH, 0.2 mm x 0.4 mm x 0.22 mm	L-05B2N7SV6T	Johanson Technology



	Components	Product number	Vendor information
LED	465 nm, 0.22 mm x 0.27 mm x 0.05 mm	C460TR2227-0216	Cree Inc.
C1,3	Capacitor, 1 pF, 0.2 mm x 0.4 mm x 0.22 mm	250R05L1R0BV4T	Johanson Technology
C2	Capacitor, 5 pF, 0.6 mm x 0.3 mm x 0.33 mm	250R05L5R1CV4T	Johanson Technology
I1	Schottky diode, 1.7 mm x 1.5 mm x 0.5 mm	1PS66SB82,115	NXP Semiconductor
L1	Inductor, 2.7 nH, 0.2 mm x 0.4 mm x 0.22 mm	L-05B2N7SV6T	Johanson Technology

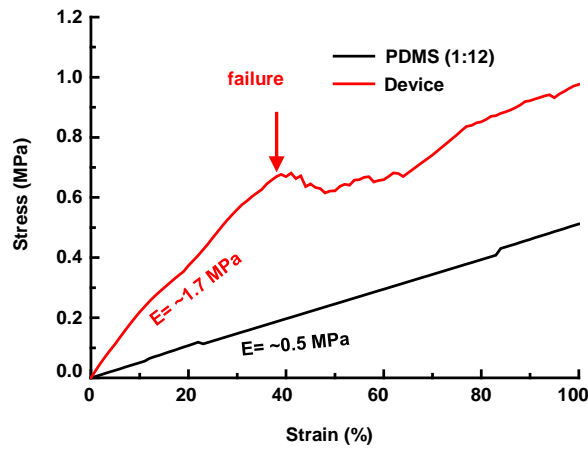
Supplementary Fig. 1 Component information for the sciatic and epidural LED devices.

Layout and component information of (a) Sciatic and (b) spinal epidural devices.



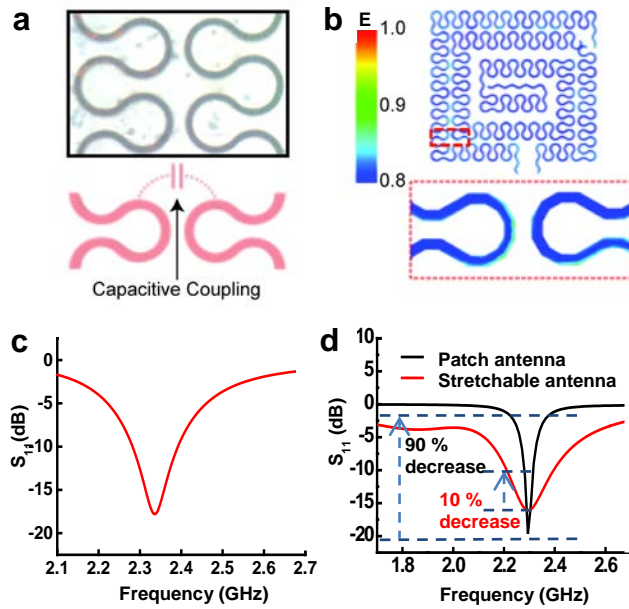
Supplementary Fig. 2

Overview of system characteristics. (a) Comparison of the emission spectrum of blue LEDs used in the devices and the absorption spectrum of Channelrhodopsin (ChR2). (b) Current-Voltage (I-V) characteristics of LEDs. (c) Light output power of the LEDs as a function of electrical input current.



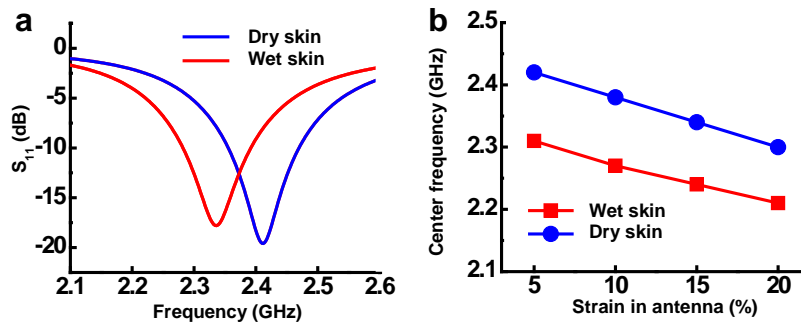
Supplementary Fig. 3

Mechanical stress limits of wireless LED devices. Stress-strain curves of the PDMS layer alone (black) and the complete implantable devices (red) under up to 100 % stretching using a Q800-DMA. The PDMS alone has a Young's modulus of 0.5 MPa with stretching of up to 100 %, while the implantable device has a Young's modulus of ~ 1.7 MPa with stretching of up to 40 % before operation failure occurs.



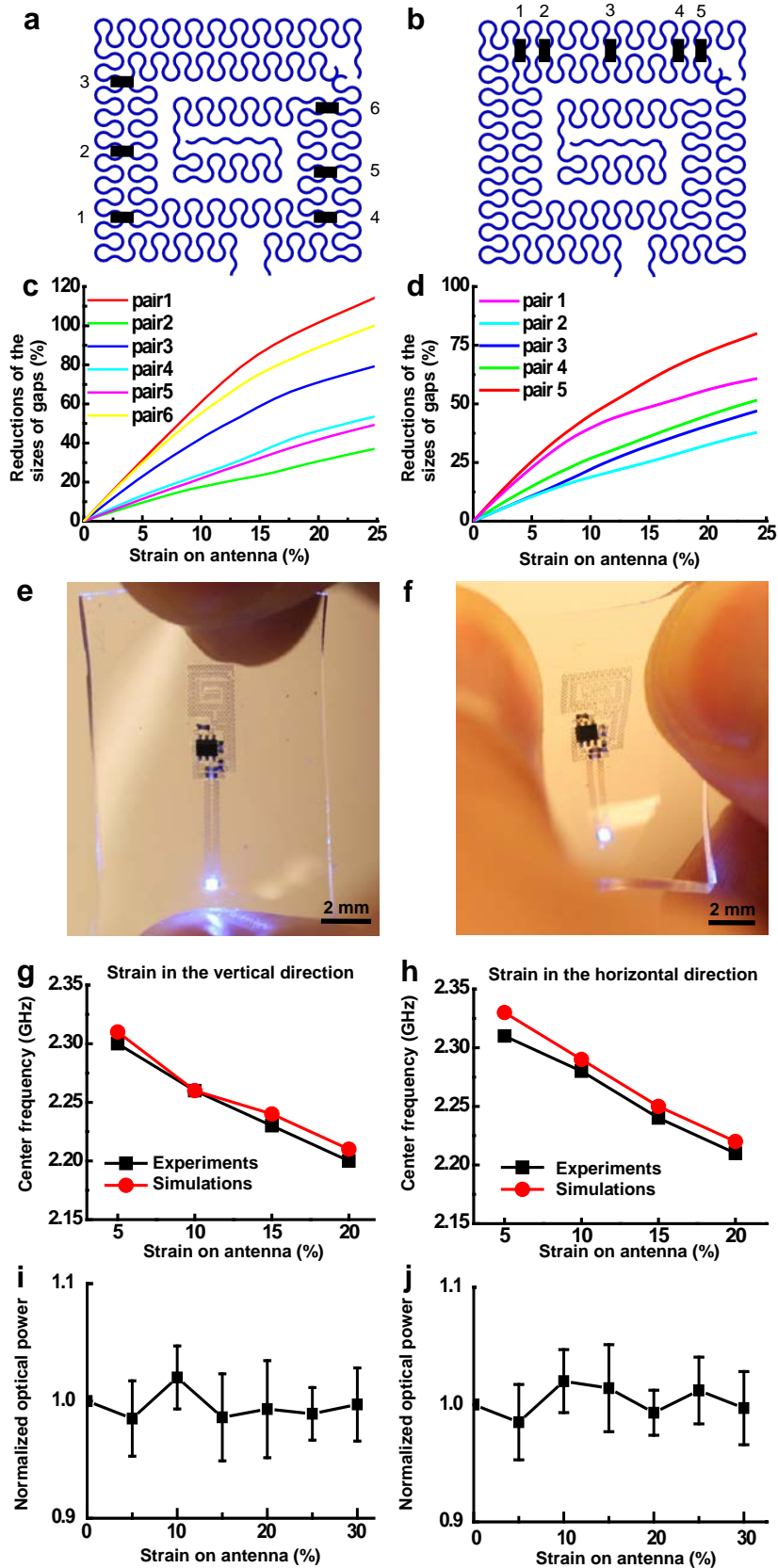
Supplementary Fig. 4

Capacitive coupling performance of stretchable antennae. (a) Exploded view of a stretchable antenna (top), schematic view of constituent serpentine wires (bottom). (b) Normalized electric field distributions on a stretchable antenna (top) and exploded view (bottom). (c) Scattering parameter, S_{11} , of a stretchable antenna in its undeformed configuration as a function of transmission frequency. (d) Comparison of the S_{11} of a stretchable antenna (red) and patch antenna (black). The bandwidth of the center frequency of the stretchable antenna (200 MHz) is significantly wider than that of the patch antenna (~50 MHz).



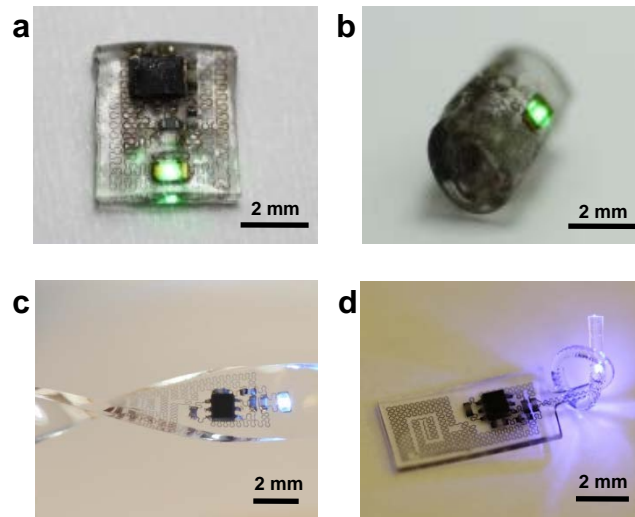
Supplementary Fig. 5

Characteristics of the stretchable antenna under wet and dry skin. (a) The scattering parameter, S_{11} , of the stretchable antenna under wet skin (red) and dry skin (blue). (b) Deviations of the center frequencies as a function of strain under wet skin (red) and dry skin (blue).



Supplementary Fig. 6

Mechanical characteristics of the stretchable antenna under strain. Mechanical characteristics of the stretchable antenna when strain is applied in the vertical direction (a), (c), (e), and (g), and in the horizontal direction (b), (d), (f), and (h). (a) Six, (b) five pairs of serpentine lines (modeled pairs are labeled with black bars) were selected to model the effects of the vertical or horizontal strain, respectively. (c), (d) Plots of gap variations versus strain on the antenna. (e), (f) Images of the stretched devices. (g), (h) Plots of center frequency versus strain on antenna based on both experiments (black) and simulations (red). (i), (j) Plots of normalized optical output power versus strain on the antenna.



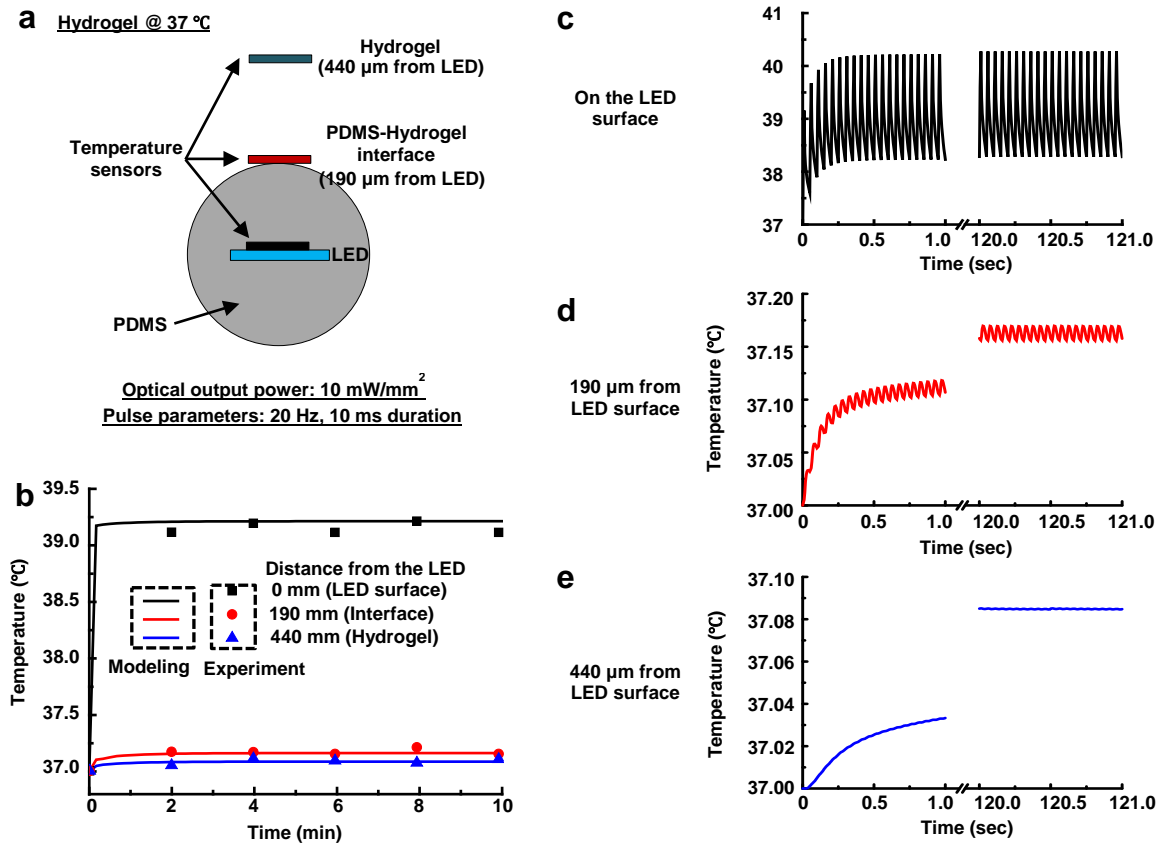
Supplementary Fig. 7

Performance of wireless LED devices under significant physical strain. Demonstrations of wireless operation when a harvester is completely folded in half (a), rolled up with a curvature of 500 µm (b), twisted (c), and knotted with a diameter of 380 µm (d).



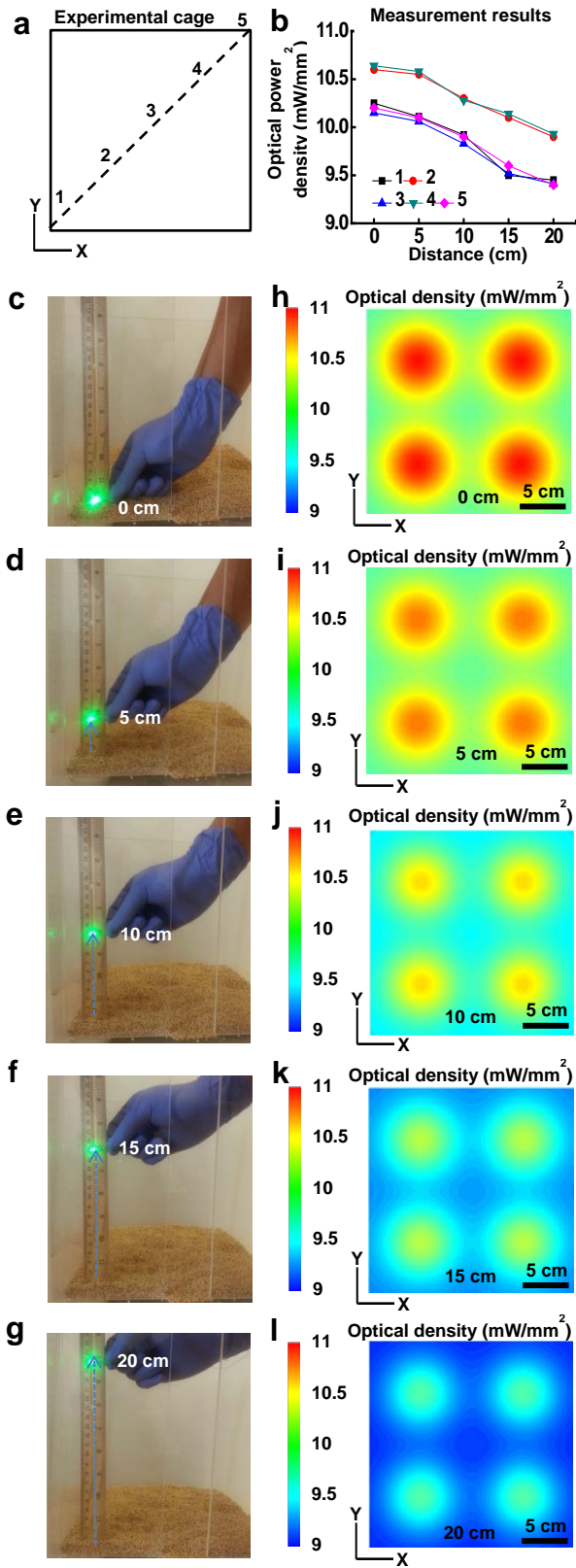
Supplementary Fig. 8

Image of a mouse with a green LED during exercise on a running wheel.



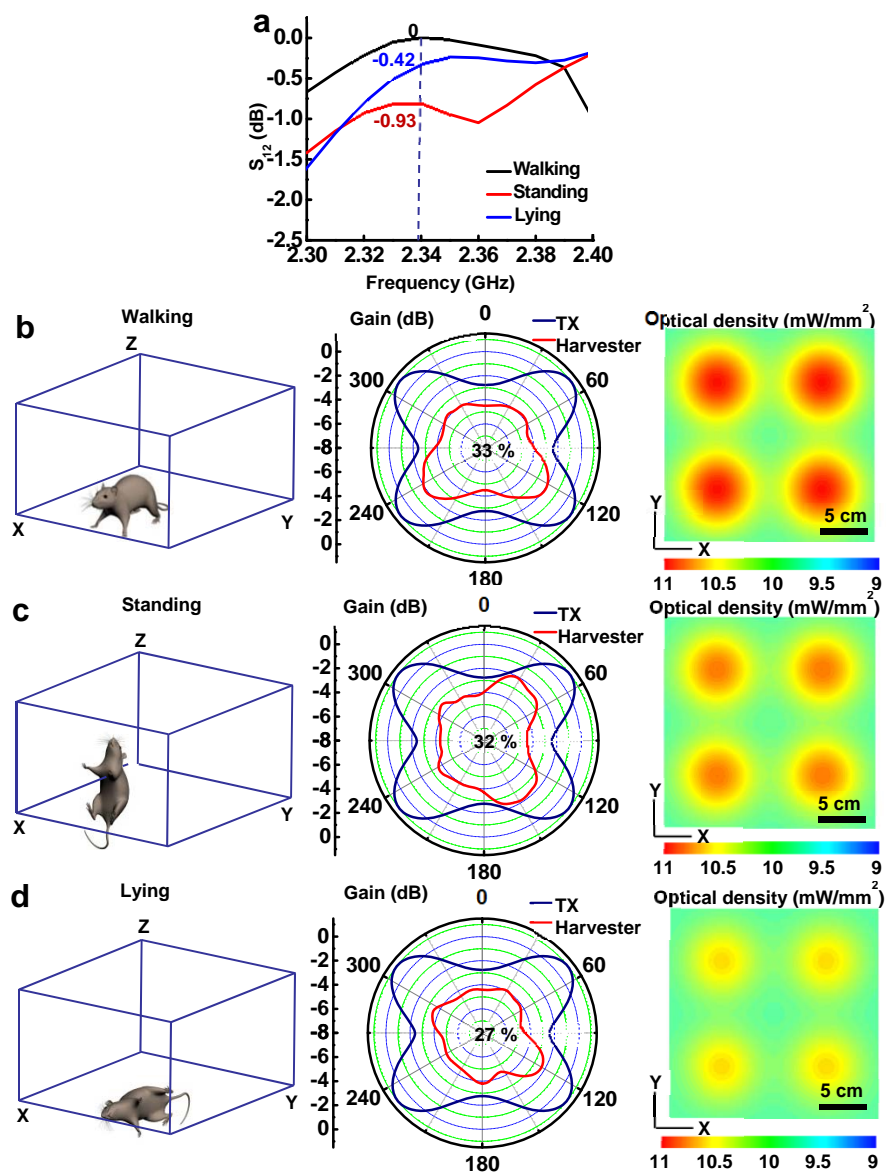
Supplementary Fig. 9

Thermal characteristics of the fully implantable LED devices. Variations of temperature were monitored at various distances (0 μm , 190 μm , or 440 μm) from the heating source (the LEDs). (a) Schematic illustration of temperature measurement, (b) Experimental and modeling results based on the distance from the LED, (c) Temperature on the surface of the LEDs from 1 to 121 seconds after activation (d) Temperature 190 μm away from the LEDs from 1 to 121 seconds after activation (e) Temperature 440 μm away from the LEDs from 1 to 121 seconds after activation.



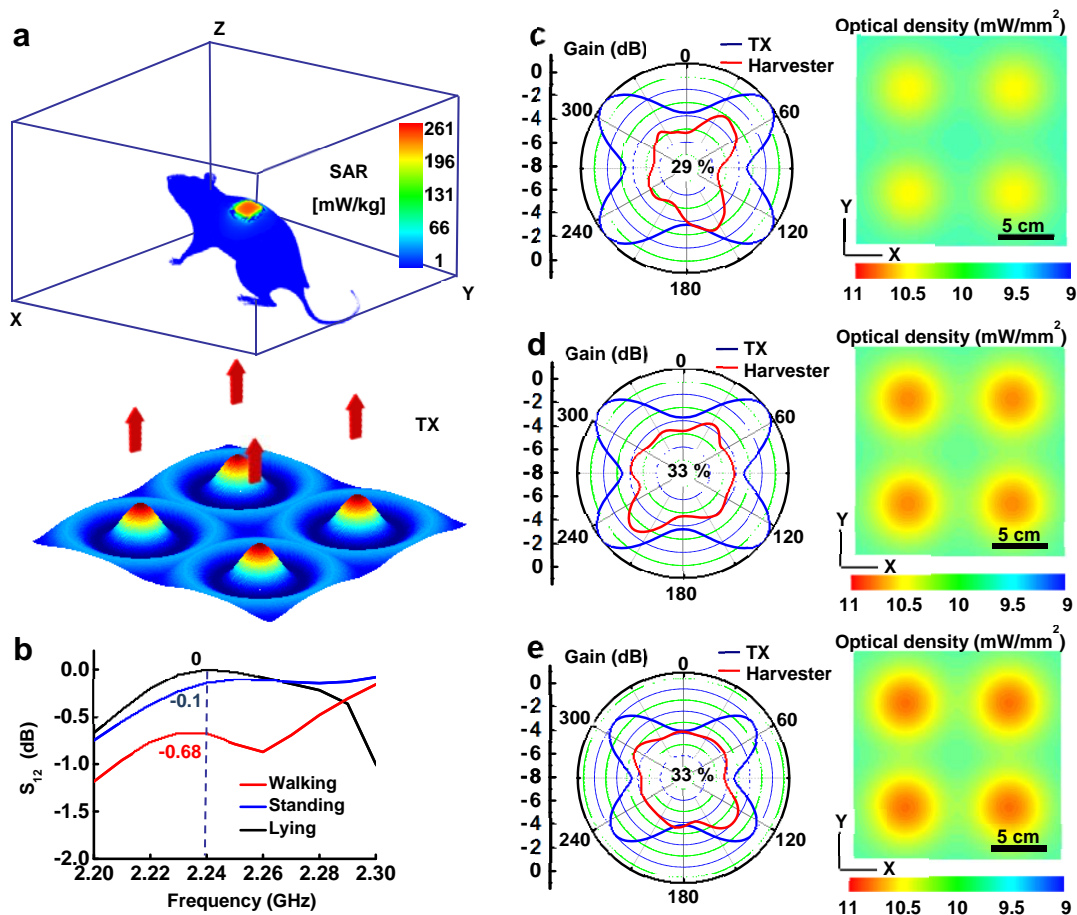
Supplementary Fig. 10

Wireless activation range for devices. (a) Illustration of locations along the cage base where the optical power density was measured. (b) Plot of measured optical power density along the black dotted line at regions 1, 2, 3, 4, and 5. (c)-(g). Images of wireless device operation in a cage at distances of 0, 5, 10, 15, and 20 cm from the antenna underneath the bottom of the cage. (h)-(l) Maps of simulated optical power densities at a distance of 0, 5, 10, 15, and 20 cm from the bottom of the cage.



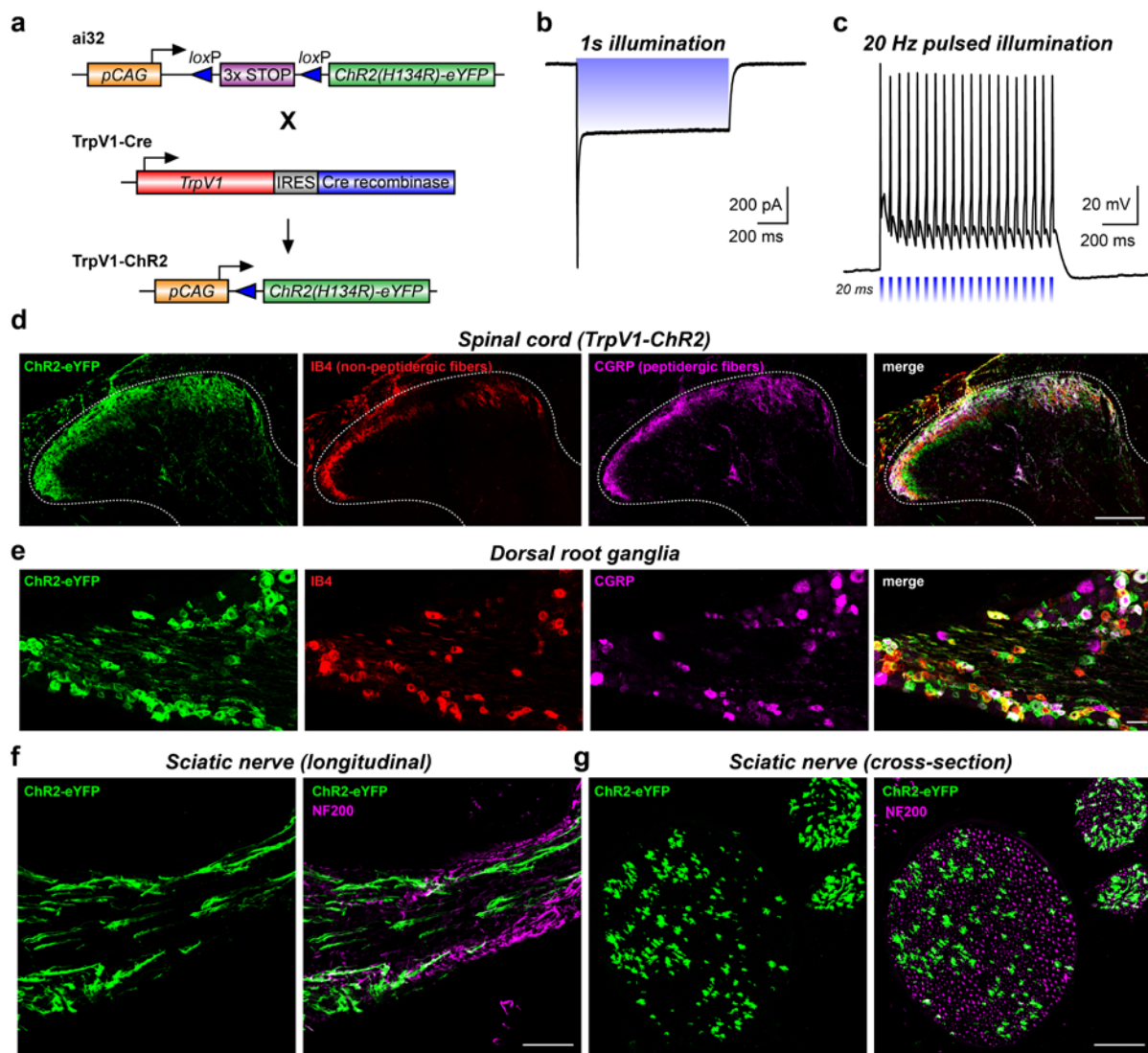
Supplementary Fig. 11

Overview of RF control strategies for peripheral nerve stimulation. (a) S_{12} as a function of frequency when a mouse walks, stands on its hind legs, and lies on its side. (b), (c), and (d) Illustrations of mouse orientation (left), corresponding angular radiation beam patterns (middle: TX system - blue, implanted harvester antennas - red), and associated simulated optical power density (right) when a mouse walks, stands on its hind legs, and lies on its side. The percentile values in the center of the plots of the angular radiation patterns indicate the extent of overlap of radiation patterns of the TX antenna and the harvester antenna.



Supplementary Fig. 12

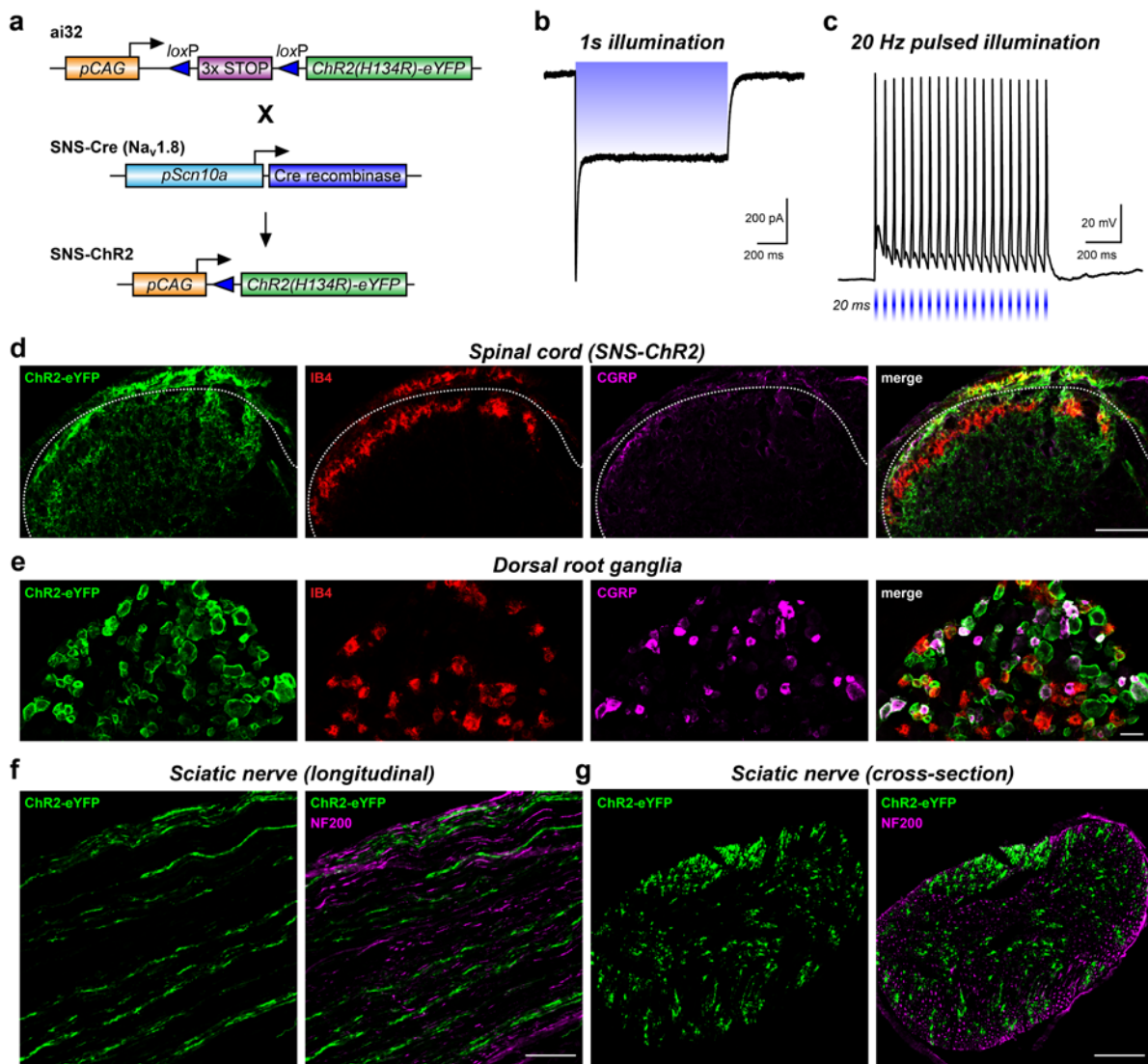
Overview of RF control strategies for spinal cord stimulation. (a) Schematic view of the TX system and an experimental assay with SAR distributions on a mouse mesh body. Multiple antennas are located on the XY plane and placed below the assay. (b) Transmission characteristics, S_{12} , of the TX system at 2.24 GHz when the mouse walks, stands on its hind legs, and lies on its side. (c), (d) and (e) Angular radiation patterns (left: TX system - blue, implanted harvester - red), and associated simulated optical power density (right) when the mouse walks, stands on its hind legs, or lies on its side. The percentile values in the center of the plots of the angular radiation patterns indicate the extent of overlap of radiation patterns of the TX antenna and the harvester antenna.



Supplementary Fig. 13

Electrophysiological and anatomical characterization of ChR2 expression in TrpV1-Ai32 mice. (a) Schematic of the Ai32 locus and TrpV1-Cre locus, together with results of the cre-dependent recombination of the Ai32 locus. (b) Inward current in cultured sensory neuron from the TrpV1-ChR2 mice. (c) In current clamp, 20 Hz pulsed illumination results in high-fidelity action potential firing in TrpV1-ChR2 mice. (d) Immunohistochemical analysis of tissue from adult TrpV1-Ai32 mice demonstrates that ChR2 is expressed along the peripheral neuraxis, including termination in lamina I and lamina II of the spinal cord dorsal horn as evidenced by overlap with CGRP (purple) and IB4 (red), respectively. (e) Staining of DRG demonstrates significant overlap of expression with CGRP (purple) and IB4 (red) within the soma, and longitudinal (f) and cross

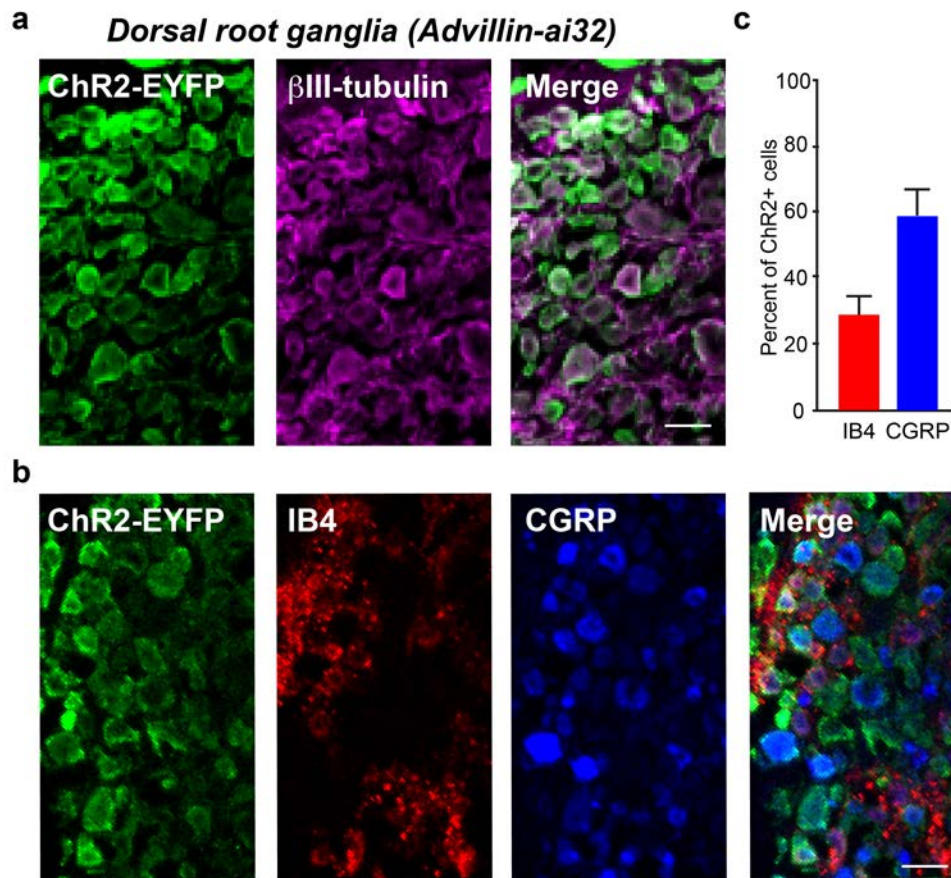
sections (g) of sciatic nerve demonstrate robust staining along the plasma membrane of the axons. This expression pattern, as expected is more restricted than in Advillin-Ai32 mice. Scale bars = 100 μm .



Supplementary Fig. 14

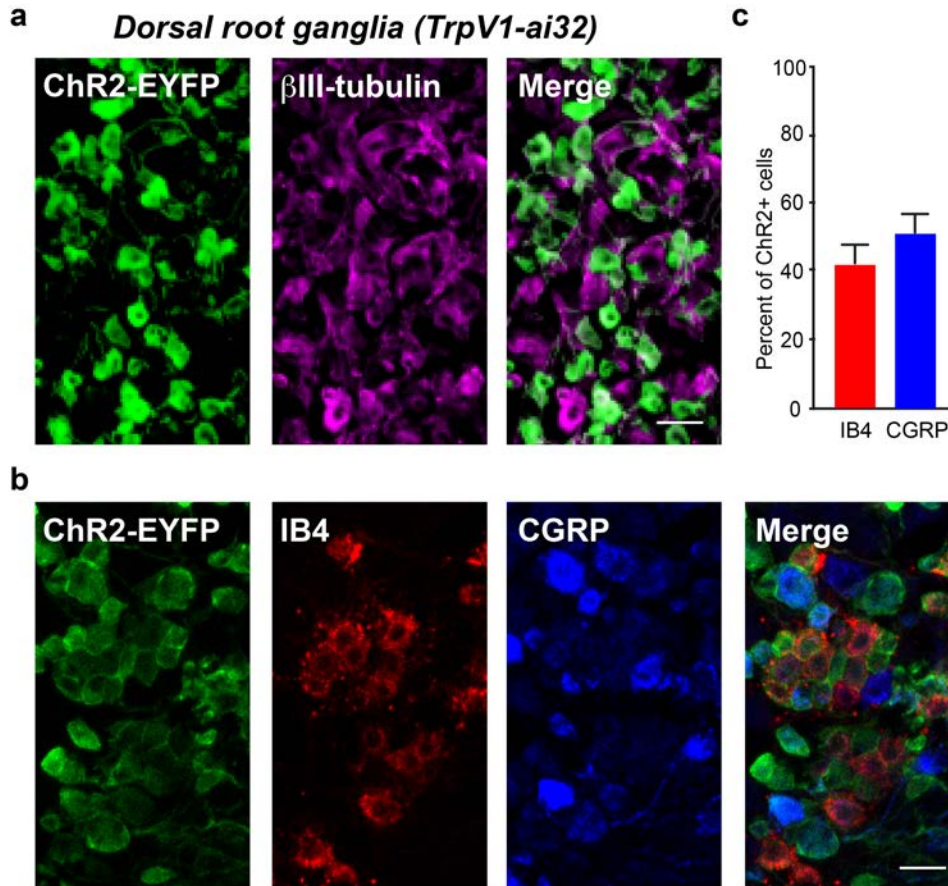
Electrophysiological and anatomical characterization of ChR2 expression in SNS-Ai32 mice. (a) Schematic of the Ai32 locus and SNS-Cre locus, together with results of the cre-dependent recombination of the Ai32 locus. (b) Inward current in cultured sensory neurons from the SNS-ChR2 mice. (c) In current clamp, 20 Hz pulsed illumination results in high-fidelity action potential firing in SNS-ChR2 mice. (d) Immunohistochemical analysis of tissue from adult SNS-Ai32 mice demonstrates that ChR2 is expressed along the peripheral neuraxis, including termination in lamina I and lamina II of the spinal cord dorsal horn as evidenced by overlap with CGRP (purple) and IB4 (red), respectively. (e) Staining of DRG demonstrates significant overlap

of expression with CGRP (purple) and IB4 (red) within the soma, and longitudinal (f) and cross sections (g) of sciatic nerve demonstrate robust staining along the plasma membrane of the axons. This expression pattern, as expected is more restricted than in Advillin-Ai32 mice. Scale bars = 100 μ m.



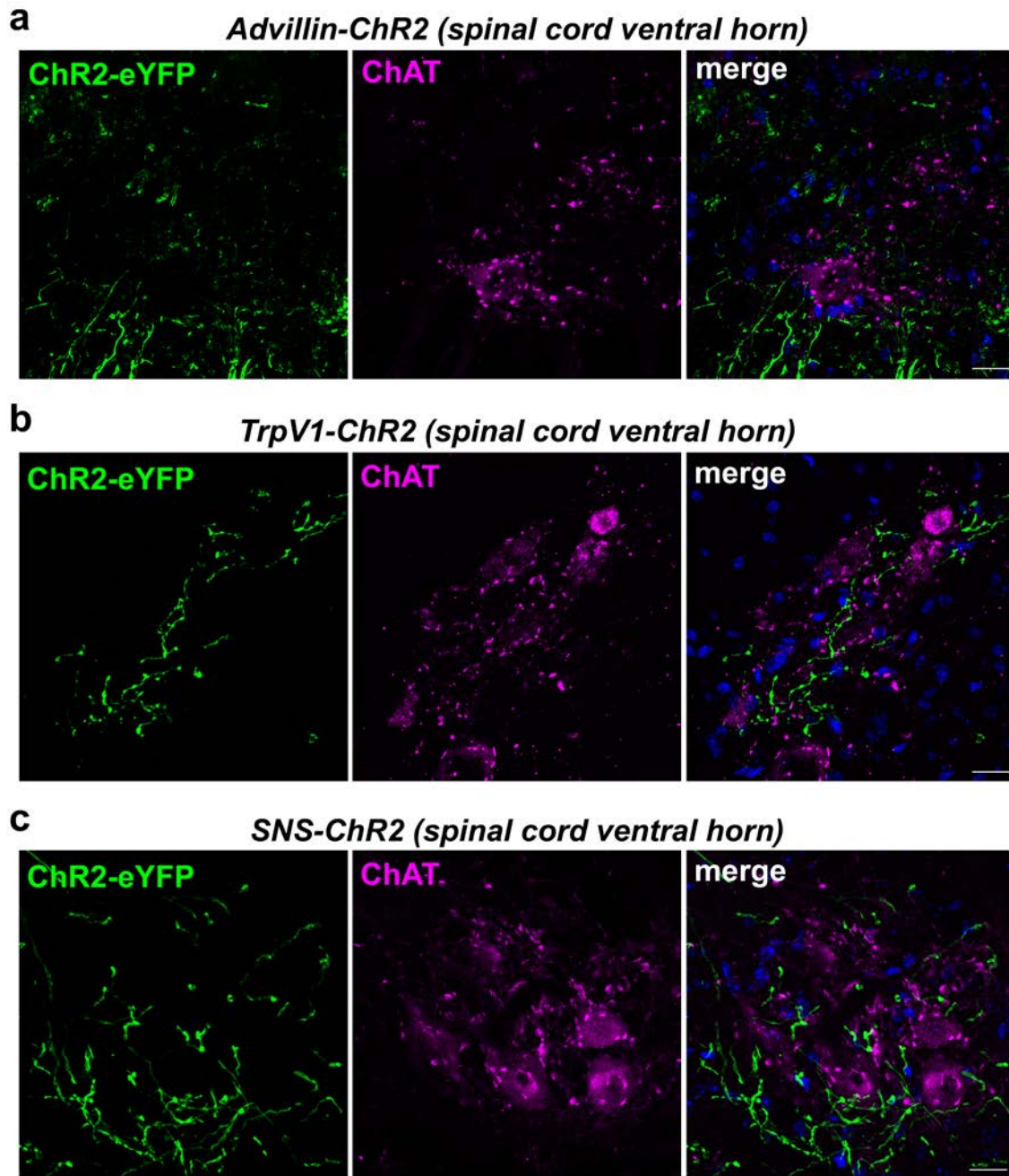
Supplementary Fig. 15

Immunohistochemical characterization of dorsal root ganglion ChR2 expression in Advillin-ChR2 mice. (a) Immunohistochemical analysis of DRG from adult Advillin-Ai32 mice demonstrates significant overlap ($82\% \pm 3\%$) of ChR2-EYFP (green) expression with β III tubulin (purple) within the soma. (b) Staining of DRG demonstrates the expression of ChR2-EYFP (green) within the subpopulation of non-peptidergic neurons, identified through labeling for IB4 (red), and subpopulation of peptidergic neurons, identified through labeling for CGRP (blue). (c) Quantification of the ChR2-EYFP expressing neurons shows that $29 \pm 6\%$ of ChR2 positive neurons co-label with the non-peptidergic population and $57 \pm 8\%$ co-label with the peptidergic (CGRP) population. Scale bars = $50\ \mu\text{m}$.



Supplementary Fig. 16

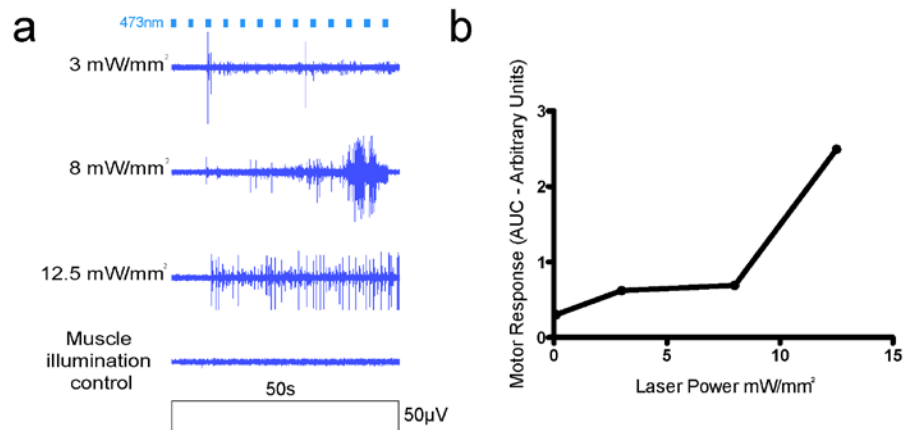
Immunohistochemical characterization of dorsal root ganglion ChR2 expression in TrpV1-ChR2 mice. (a) Immunohistochemical analysis of DRG from adult TrpV1-Ai32 mice demonstrates significant overlap (59 ± 3 %) of ChR2-EYFP (green) expression with β III tubulin (purple) within the soma. (b) Staining of DRG demonstrates the expression of ChR2-EYFP (green) within the subpopulation of non-peptidergic neurons, identified through labeling for IB4 (red), and subpopulation of peptidergic neurons, identified through labeling for CGRP (blue). (c) Quantification of ChR2-EYFP expressing neurons shows that 41 ± 5 % of ChR2 positive neurons co-label with the non-peptidergic (IB4) population and 51 ± 7 % co-label with the peptidergic (CGRP) population. Scale bars = 50 μ m.



Supplementary Fig. 17

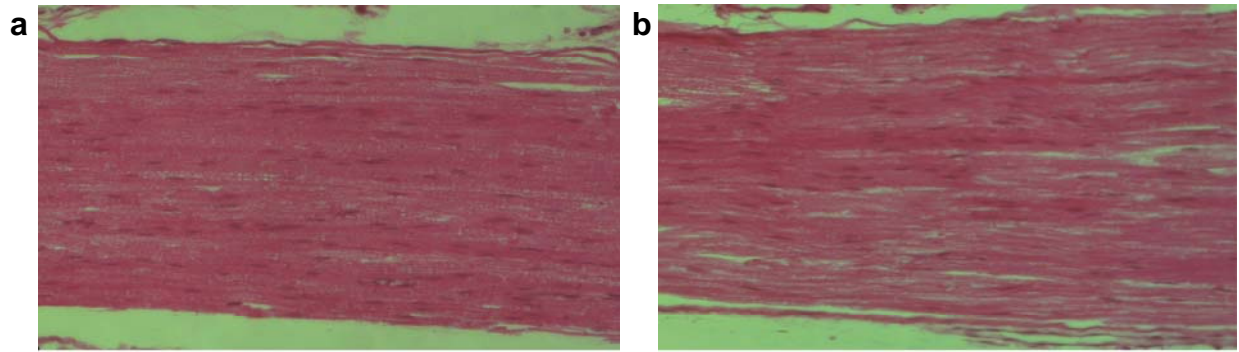
Characterization of ChR2-EYFP expression in the ventral horn of the spinal cord of Advillin-ChR2, TrpV1-ChR2, and SNS-ChR2 mice. Confocal images of the spinal cord ventral horn from Advillin-ChR2 (a), TrpV1-ChR2 (b) and SNS-ChR2 (c) mice, showing sparse ChR2⁺ fibers (green) innervating deeper lamina. Motor neurons are marked by choline acetyltransferase

(ChAT, purple). We did not observe ChR2 expression in motor neurons of any of these transgenic lines. The scale bar indicates 20 μm for all panels.



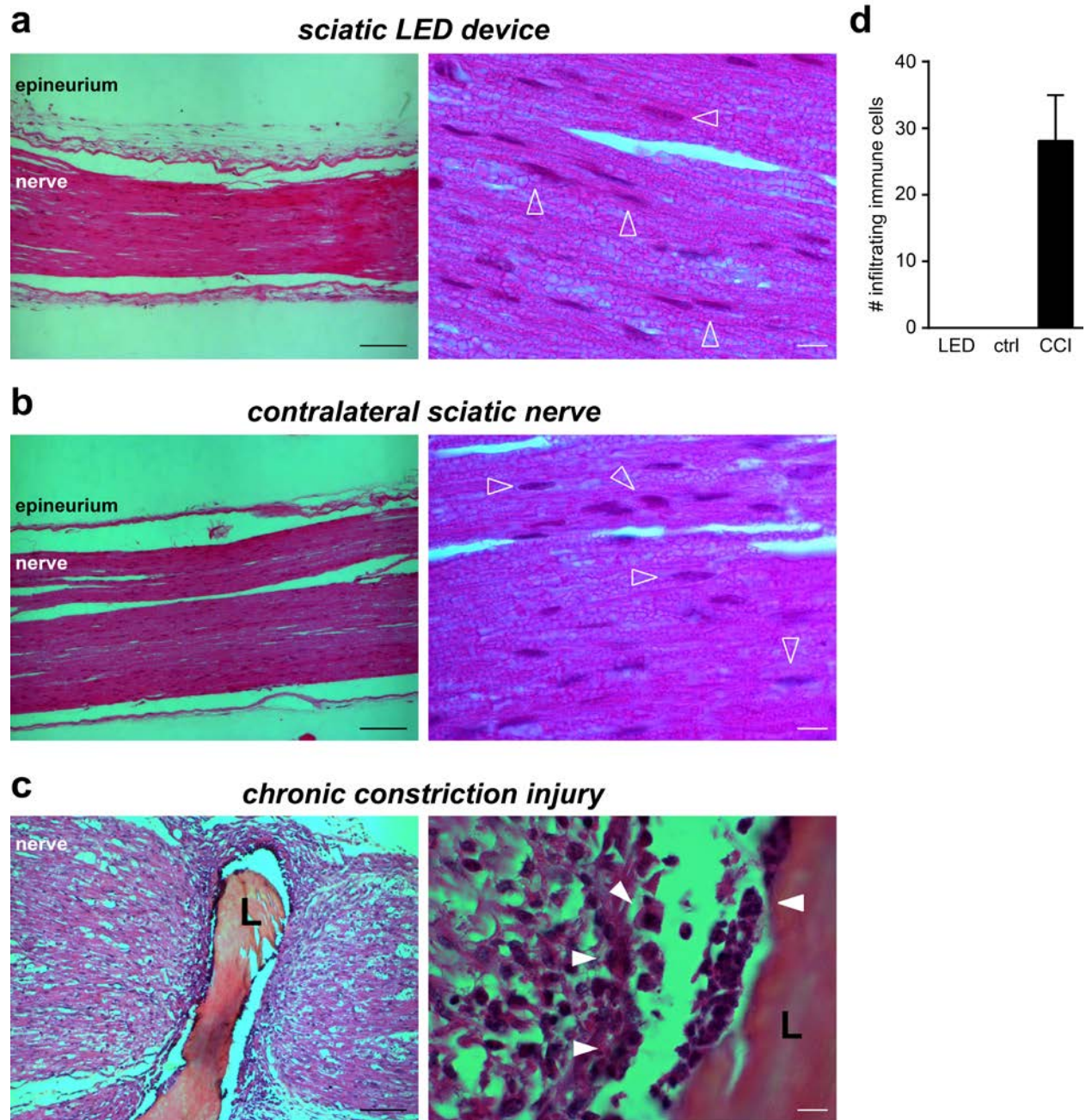
Supplementary Fig. 18

Direct laser activation of the sciatic nerve in an open preparation. Blue fiber-optic laser illumination of the exposed sciatic nerve in lightly anesthetized TrpV1-ChR2 mice produces reflexive withdrawal behaviors. (a) EMG tracing showing quadriceps contractions during blue-laser illumination of the exposed sciatic nerve ranging between 3 - 12.5 mW/mm². In the bottom trace, the laser illuminated the muscle on top of the sciatic nerve, but not the nerve itself and evoked no motor response. This is consistent with the muscle contractions being a reflexive response to optogenetic excitation of the axons by blue light. (b) Quantification of the EMG recordings from the quadriceps during laser illumination of the sciatic. Motor response (area under the curve – arbitrary units) increased as the laser power increased.



Supplementary Fig. 19

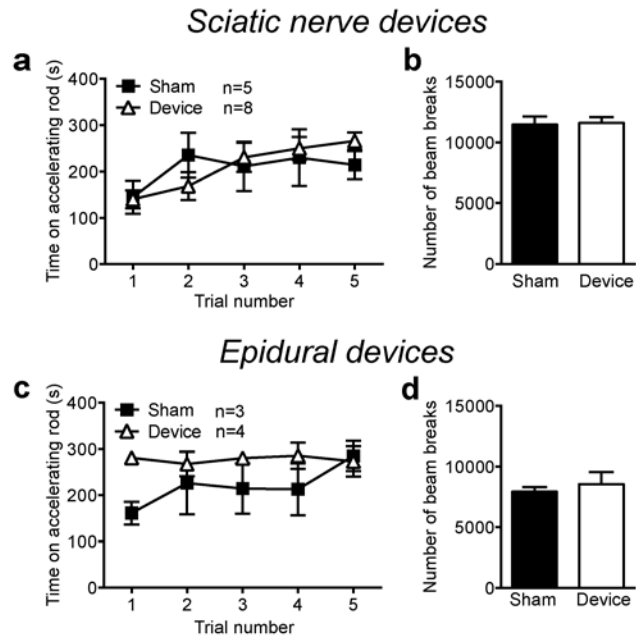
Hematoxylin and eosin (H&E) staining of sciatic nerves taken from C57BL/6J wild type mice at 16x magnification. (a) is a representative ipsilateral nerve which has been interfaced with the sciatic optogenetic simulator for 1 month. (b) is the contralateral nerve from the same animal utilized for comparison. No gross infiltration was noted using standard H&E techniques to observe neutrophils, lymphocytes, monocytes, basophils, eosinophils, red blood cells, or lipofuscin.



Supplementary Fig. 20.

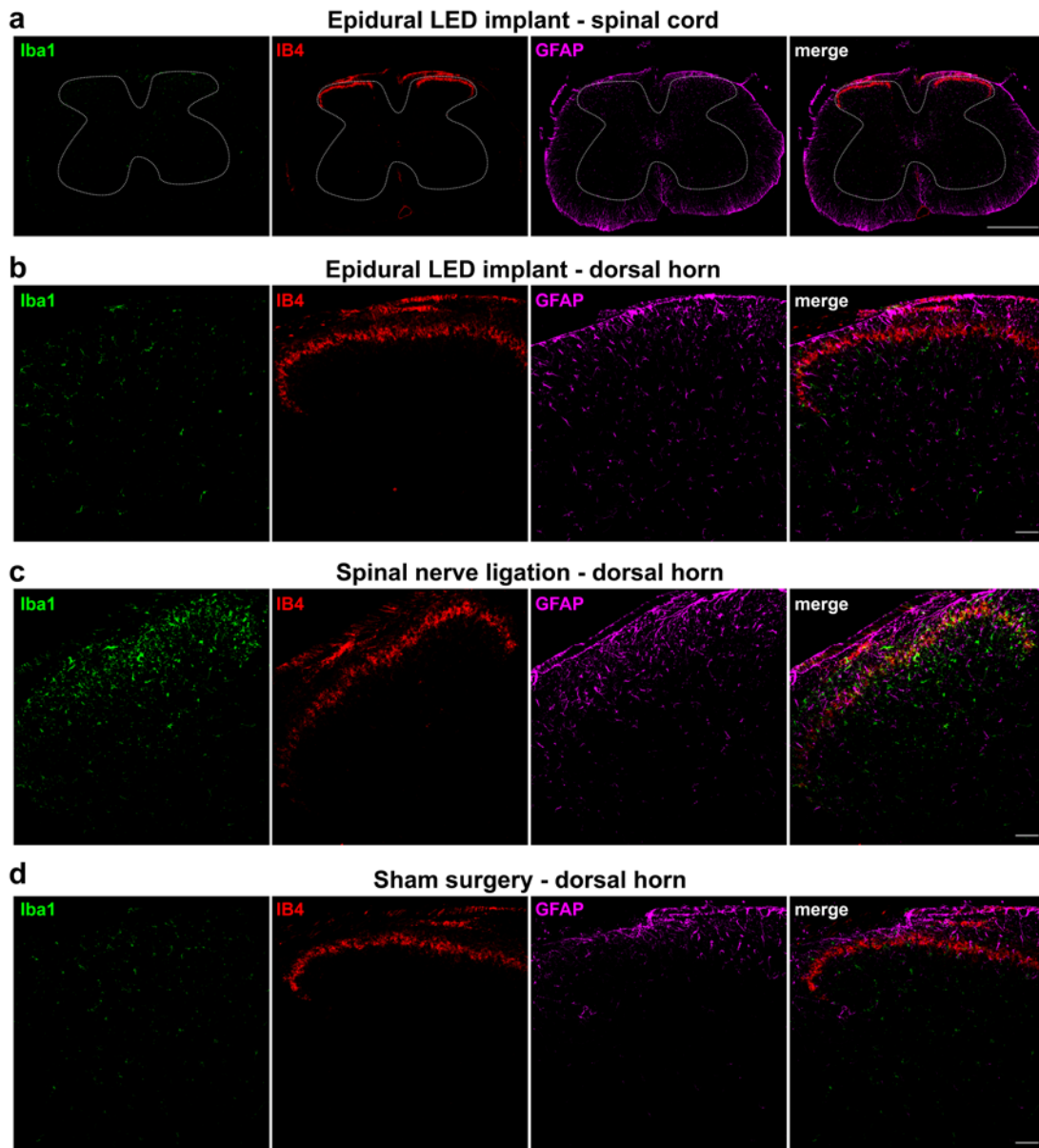
Histological analysis of the sciatic nerve after peripheral nerve device implantation or the chronic constriction injury procedure. (a)-(c) Transmitted light micrographs of haematoxylin (purple) and eosin (pink) staining of longitudinal sciatic nerve sections taken at 10x (left) and 63x (right). Panels in (a) show sections of the sciatic nerve from a mouse with a peripheral device implanted for 2 weeks. The LEDs were positioned in the middle of this section of nerve.

Open arrowheads highlight the flattened nuclei of myelinating Schwann cells (purple). Images in (b) are from the contralateral nerve. Sciatic nerve sections in (c) are from a mouse that had a chronic constriction injury surgery (CCI), a model for neuropathic pain. Note the large number of infiltrating immune cells, identified by their multi-lobed nuclei (closed arrowheads) surrounding the ligature (L) and the prominent swelling of the nerve due to inflammation. (d) Quantification of immune cell infiltration in 63x images of the sciatic. No immune cells were identified in device-implanted animals (LED), the contralateral control sections (ctrl). However we observed 28 ± 7 immune cells per section from CCI mice. Quantification was performed on 2 - 4 sections from 3-4 mice for each condition; data represent mean \pm sem. Scale bars are 100 μ m for 10x images and 10 μ m for 63x images.



Supplementary Fig. 21

Characterization of locomotor activity after sciatic and epidural device implantation using the open field and accelerating rotarod tests. (a) Accelerating rotarod testing of C57BL/6J wild type mice implanted with sciatic nerve devices ($n = 8$) versus sham-operated littermates ($n = 5$) at one week post-implantation. Two-way ANOVA revealed no significant difference ($p = 0.891$) between the two groups. (b) Open field testing of locomotor activity of C57BL/6J wildtype mice implanted with optogenetic sciatic nerve stimulators ($n = 8$) versus sham-operated littermates ($n = 5$) at one week post-implantation. A T-test revealed no significant difference between the two groups ($p = 0.886$). (c) Accelerating rotarod testing of C57BL/6J wild type mice implanted with epidural devices ($n = 4$) versus sham-operated littermates ($n = 3$) at one week post-implantation. Two-way ANOVA revealed no significant difference ($p = 0.226$) between the two groups. (d) Open field testing of locomotor activity of C57BL/6J wild type mice implanted with epidural devices versus sham-operated littermates at one week post-implantation ($n = 3$ per group). A T-test revealed no significant difference between the two groups ($p = 0.589$).



Supplementary Fig. 22

Immunohistological analysis of the dorsal horn of the spinal cord after either epidural device implantation or the spinal nerve ligation procedure. (a) Low power confocal micrograph of a transverse section of the lumbar spinal cord from a mouse with an epidural LED device implanted in the epidural space for two weeks. Iba1 (green) labels activated microglia, IB4 (red) labels non-peptidergic sensory afferents in lamina II of the dorsal horn, and GFAP (purple) marks astrocytes. The dotted line outlines the spinal cord gray matter. Scale bar is 500 μ m. (b) Higher power confocal images of the dorsal horn of the lumbar spinal cord from a mouse with an

epidural LED device implanted for two weeks. Sections were labeled for markers of activated microglia (Iba1, green), non-peptidergic fibers in the dorsal horn (IB4, red), and astrocytes (GFAP, purple). We did not observe the presence of activated microglia or proliferating astrocytes in implanted mice. Scale bar is 50 μm . (c) Spinal cord dorsal horn sections five days after ligation of the L4 spinal nerve. Notice the prominent labeling of activated microglia (green) and astrocyte proliferation (purple). Scale bar is 50 μm . (d) Spinal cord dorsal horn sections from a mouse that underwent a laminectomy but was not implanted with an epidural LED device. We did not detect prominent activation of microglia or increased astrocyte proliferation following the simple laminectomy. Scale bar is 50 μm .

Process	Purpose	Required time for 10 devices	Equipment	Progress level (%)
1. Preparation of PMMA coated glass	Sampling for transfer	1 hour	Cleanroom Spin-coater	5
2. PI film fabrication	Bottom encapsulating layer	3 hours	Cleanroom, Vacuum oven	15
3. Metal (Ti/Au) deposition	Interconnection	3 hours	E-beam deposition	25
4. Metal patterning		2 hours	Cleanroom, Mask aligner	30
5. PI encapsulation	Top encapsulating layer	3 hours	Cleanroom, Vacuum oven	40
6. PI/Metal/PI patterning	Patterning for stretchable circuits	2 hours	Cleanroom, mask aligner,	50
7. PI etching		3 hours	RIE	60
6. Components transfer	Active components integration	5 hours	Solder, Microscope	80
7. PDMS encapsulation	System packaging	1 hour	Oven	100

Supplementary Table 1: Fabrication process details

Parameter	TrpV1-ChR2
Rise time	2.4 ± 0.2 ms
Peak amplitude	261.1 ± 53.1 pA
tau	12.5 ± 1.0 ms
Steady state	98.4 ± 20.0 pA
% Steady state	37.6 ± 0.5
APs fired in response to a 10 Hz stimulus lasting 2, 5, or 10 ms	6 ± 3
APs fired in response to a 20 Hz stimulus lasting 20 ms	7 ± 3

Supplementary Table 2: Electrophysiological properties of ChR2-expressing sensory neurons in response to optical stimuli, rise time, peak amplitude, tau, steady state and percent steady state. These parameters are based on a 470 nm, 10 mW/mm² light pulse that was 1s in length (n = 9). The number of action potentials fired to a 10 Hz stimulus is a result of pooling the responses to 470 nm, 10 mW/mm² light pulses lasting either 2, 5 or 10 ms in length (n = 4). The number of action potentials fired to a 20 Hz stimulus is a result of a 470 nm, 10 mW/mm² light pulse 20 ms in length (n = 6). AP; action potential. Data are presented as mean ± standard error of the mean.

Supplementary Movie 1: Device implantation does not inhibit exercise behavior

Clip of a mouse with a green sciatic nerve LED device running on an exercise wheel without any limitations.